LIDAR-assisted nonlinear output regulation of wind turbines for fatigue load reduction

Robert H. Moldenhauer[1] and Robert Schmid[1]

[1]Department of Electrical and Electronic Engineering, University of Melbourne

Correspondence: Robert H. Moldenhauer (moldenhauer.r@student.unimelb.edu.au)

Abstract.

Optimizing wind turbine performance involves maximizing or regulating power generation while minimizing fatigue load on the tower structure, blades, and rotor. In this article, we explore the application of a novel turbine control methodology known as nonlinear output regulation (NOR) for improving turbine control performance. NOR uses a multiple-input-multiple-output design approach to regulate rotor speed and power generation with the generator torque and blade pitch angles, in a unified manner across partial and full load operation. Regulation is achieved using an estimate of rotor-effective wind speed. We consider estimation based on the turbine's SCADA, in particular the Immersion & Invariance (I&I) estimator, as well as LIDAR. We propose to average these two signals to obtain a low-variation real-time estimate of current wind speed.

The performance of the NOR controller is compared against a state-of-the-art baseline reference controller, known as ROSCO. Extensive simulations of the NOR and ROSCO controllers using openFAST on an IEA 15-MW reference turbine, across a broad range of wind speeds in both partial load and full load operating regions are conducted. Results show that NOR with the combination of I&I and LIDAR improves on all considered performance metrics. Lifetime damage-equivalent loads are reduced on the tower by 2.6% fore-aft and 11.6% side-to-side, on the blades by 4.7% flapwise and on the main shaft by 15.2%. Furthermore, pitch rate is reduced by 22.6%. The reductions are achieved without sacrificing power generation or tracking performance.

1 Introduction

Wind energy conversion systems are one of the most cost-effective and widely used sources of renewable energy. A 2021 study by Fraunhofer ISE (Bundesverband der Energie- und Wasserwirtschaft, 2023) put the levelised cost of energy (LCOE) for wind energy in Germany at 3.94-8.29 eurocents per kWh, which is about half the LCOE of lignite, hard coal and gas turbines (Kost et al., 2021). In 2022 wind energy accounted for 21.7% of energy production in Germany. The fastest growing market is China, where market volume of wind energy is expected to grow from $443.74\,\mathrm{GW}$ in 2023 to $772.64\,\mathrm{GW}$ in 2028 (Mordor Intelligence, 2024).

Over recent years, upwind, three-bladed, horizontal-axis variable-speed and variable-pitch wind turbines have become the predominant type (Gambier, 2022). The grid connection of variable-speed turbines is realized with power converters. With electronics the generator torque can be controlled, which affects the energy that is extracted from the rotor, and therefore how

much it is accelerated or decelerated. Variable-pitch refers to the availability of blade pitch actuation, with the main purpose of decreasing energy capture at high wind speeds for safety. The primary control objective is to maximize power capture at lower wind speeds, and to not excessively exceed rated power at higher wind speeds. This can be achieved with fairly simple control methods, and more sophisticated methods can provide only marginal power capture improvements. An important secondary

30 control objective is fatigue load reduction. As wind is inherently turbulent, tower and blades are subject to ever-changing stress and strain, which causes mechanical fatigue. Furthermore, the blade pitch actuation is susceptible to wear and tear. These factors are the reason why wind turbines generally have a lifespan of only around 20 years. Therefore, the reduction of fatigue loads and actuator usage through control has the potential to make wind turbines more durable and further decrease their LCOE.

35 Control methods for improving turbine performance have been subject of extensive research for at least five decades, and summaries are available in the monographs (Bianchi et al., 2007; Munteanu et al., 2008; Luo et al., 2014; van Kuik and Peinke, 2016; Gambier, 2022), for example. For a very recent survey on control methods for wind turbine fatigue load reduction, see (Yaakoubi et al., 2023). Such methods may be broadly separated into strategies for life-of-turbine operating methods that seek to improve turbine life-span by derating, or even shutting down, the turbine in certain operating conditions, and real-time

40 control methods that seek to achieve maximum power point tracking (MPPT) or rated power generation while designing the control actuation in a manner that reduces strain on the tower, blades and generator. Papers in the first category include (Bech et al., 2018), who sought to identify extreme precipitation events causing the largest impact on turbine blade fatigue loads. Operational strategies to find suitable trade-offs between fatigue loads and power production in the long-term management of a wind farm have been investigated in (Requate et al., 2023) and (Kipchirchir et al., 2023).

45 In this paper we give our attention to the second category of controller methodologies, in which conventional control methods for MPPT are augmented to reduce fatigue loads. According to a 2016 review about the state of the art and future challenges of wind turbine control, the industry standard is to use single-input-single output (SISO) gain-scheduled PID-regulators (van Kuik and Peinke, 2016, Chapter 4). The Reference Open-Source Controller (ROSCO) (Abbas et al., 2022) was recently developed to provide a modular reference wind turbine controller that represented industry standards and was shown to provide better

50 performance than existing reference controllers, in particular the baseline controller of Jonkman et al. (2009).

Many researchers have investigated control methodologies that use an estimate of the wind speed. Wind speed estimation can be classified into two approaches. The first approach uses the rotor speed measurement and other data available from the turbine's SCADA to compute the rotor effective wind speed (REWS), a single wind speed value representing the equivalent steady, horizontal and uniform upstream velocity. Many strategies, such as the extended Kalman filter, Immersion & Invariance

55 (I&I) estimator, and power balance estimator, have been investigated to compute the REWS estimate. See (Soltani et al., 2013) for a comparison of estimation methods.

The second approach involves external wind measurement devices, most commonly involving light detection and ranging (LIDAR) sensors, which uses lasers to measure wind speeds in front of the turbine. A detailed description of LIDAR for wind turbines can be found in (Schlipf, 2016). LIDAR-assisted control has been shown to successfully reduce fatigue loads in

60 (Schlipf et al., 2013; Fu et al., 2023).

One popular control methodology enabled by wind speed estimation is disturbance accommodation control (DAC), also known as disturbance tracking control (DTC), which was introduced by (Balas et al., 1998). DAC uses a superposition of a stabilizing feedback term and a feedforward of the disturbance estimate, aimed at disturbance rejection. If control and disturbance are matched, an equation can be solved to find a feedforward gain, which immediately compensates the disturbance. In wind turbines, drivetrain and blade pitch actuation dynamics, albeit being relatively fast, make this equation unsolvable directly. It is therefore solved approximately (Yuan and Tang, 2017), (Yaakoubi et al., 2023). DAC was also featured in (Wright, 2004) and (Wright and Fingersh, 2008). Wright et al. (2006) showed that DAC can reduce loads on the low-speed shaft in field tests, compared to a baseline controller.

Exact output regulation (EOR) is a classical linear control systems architecture that is able to track time-varying reference signals while rejecting time-varying disturbances (Saberi et al., 2000). The reference and disturbance signals are assumed to be generated by a known exosystem. EOR feedforwards the exosystem state, where the feedforward gain matrix is obtained as solution of a Sylvester equation, to asymptotically track the reference under the influence of the disturbance. In (Mahdizadeh et al., 2021) EOR was first applied for wind turbines in conjunction with LIDAR, and simulations showed significant fatigue load reduction compared to baseline controller of (Jonkman et al., 2009) and DAC. In (Woolcock et al., 2023) the I&I estimator was used instead of LIDAR, without significantly affecting the control performance.

In this paper we introduce a novel nonlinear wind turbine control design methodology, referred to as nonlinear output regulation (NOR). It employs a multiple-input-multiple-output design approach that determines generator torque and blade pitch angles in conjunction in order to regulate both rotor speed and power output. It adapts to specific requirements across varying wind speed, where in the partial load operation blade pitch angles are fixed to generate maximum power and the generator torque regulates rotor speed, while in full load operation the blade pitch actuation regulates rotor speed, all while transitioning seamlessly between the two regions.

To achieve rotor speed and power regulation, NOR uses a wind speed estimate. This allows direct inclusion of LIDAR estimates in a unified manner across operation regions. In particular, we propose to use an average of I&I and LIDAR estimates. With I&I lagging behind the actual REWS and LIDAR being a look-ahead estimate, we obtain a real-time estimate of the current wind. This average has lower variation than the individual signals because the noises affecting both estimates having different (independent) sources.

The performance of NOR was tested with openFAST (NREL, 2019) on the IEA 15-MW reference turbine (Gaertner et al., 2020). Full-field wind signals at mean wind speeds between 5 and $20\,\mathrm{m\,s^{-1}}$ were generated with TurbSim (Jonkman, 2006), in accordance with the IEC standard (IEC, 2005). The simulations consider the power generation, the fatigue loads for the tower, blades and main shaft, the blade pitch actuation and the maximum rotor speed. We use ROSCO (Abbas et al., 2022) as the baseline controller for our performance comparisons. Our results showed that the NOR controller, using the average of I&I and LIDAR wind speed estimates, was able to give average fatigue load reductions of between 2.6 and 15.3%, compared with ROSCO. The NOR controller also averaged a pitch rate reduction of 22.5% and reduced the root mean square (RMS) rotor speed tracking error by 37%. These improvements did not come at the cost of any reduction in the average power generation.

hub height	150 m
rotor radius R	120 m
rated power P_{rated}	15 MW
cut-in wind speed	$3\,\mathrm{m\,s^{-1}}$
rated wind speed v_{rated}	$10.59\,\mathrm{m\,s^{-1}}$
cut-out wind speed	$25\,\mathrm{m\,s^{-1}}$
rated rotor speed Ω_{rated}	7.56 rpm
minimum rotor speed Ω_{min}	5 rpm
optimal power coefficient $C_{p,opt}$	0.489
optimal tip speed ratio λ_{opt}	9
generator efficiency η_{gen}	96.55%

Table 1. 15-MW reference turbine parameters (Gaertner et al., 2020)

95 The paper is organized as follows: Section 2 discusses all aspects of the modelling of the 15 MW turbine considered in this study. Section 3 describes the I&I and LIDAR methods used to be used for wind speed estimation, and Section 4 describes the NOR and ROSCO control methodologies to be compared in our performance comparisons. Section 5 describes the Simulink™ simulation environment that was developed to test and compare these two control methodologies for their power generation and fatigue loads under a wide range of wind profiles. Section 6 provides the results of our simulations and discusses the relative

100 performance of NOR against ROSCO. Some final remarks are given in the Conclusion, and the Appendix contains some more theoretical analyses and comparisons of these two control methodologies.

2 Wind turbine modelling

The wind turbine model considered in this work is the IEA 15-MW reference turbine, documented in (Gaertner et al., 2020). It has a variable speed, collective pitch controller; and a low-speed, direct-drive generator. The main parameters are shown in

105 Table 1. Depending on the wind speed, four operating regions are defined. In Region 1, below cut-in speed, there is insufficient wind to power the turbine. In Region 2, which is between cut-in wind speed and rated wind peed, as much power as possible shall be produced. Above rated wind speed, the rated power of 15 MW can be produced. In Region 3, which is between rated and cut-out wind speed, due to the load capacity of mechanical components and constraints by the generator and grid connection, power output shall be near rated, without overspeeding of the rotor. Operating the turbine in Region 4 would cause

110 excessive loads, so power generation is shut down to protect the turbine. Wind speeds near rated wind speed are known to be difficult for turbine control as the power objective varies between maximum power generation and rated power.

In the following sections we develop a simplified turbine model that will be used to design the NOR controller. Performance simulations will be conducted with OpenFAST (NREL, 2019).
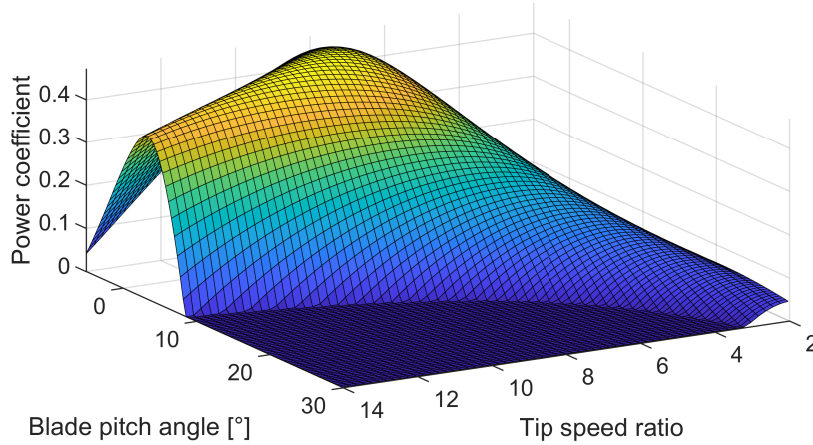
Figure 1. Power coefficient surface of the 15-MW reference turbine.

2.1 Aerodynamic torque

115 Let R denote the rotor radius and ρ the air density. The total power of uniform wind moving through the rotor disc, termed *instantaneous power*, is

$$P_{\text{wind}}(v_x) = \frac{1}{2}\rho\pi R^2 v_x^3. \tag{1}$$

where v_x is the magnitude of the horizontal component of the wind velocity vector perpendicular to the rotor plane. The power extracted from the wind by the blades is the *aerodynamic power*, and the ratio of the aerodynamic power to the instantaneous
120 power is given by the *power coefficient* $C_p(\lambda, \theta)$. It depends on the tip speed ratio

$$\lambda = \frac{R\Omega}{v_x}, \tag{2}$$

where Ω denotes the rotor speed, and the blade pitch angle θ. The power coefficient surface of the 15-MW reference turbine is shown in Figure 1. The maximal power coefficient $C_{\text{p,opt}} = 0.489$ is achieved at optimal tip speed ratio $\lambda_{\text{opt}} = 9$ and $\theta = 0°$. The aerodynamic power and aerodynamic torque are

125 $$P_a(\Omega, v_x, \theta) = \frac{1}{2}C_p(\lambda, \theta)\rho\pi R^2 v_x^3, \tag{3}$$

$$M_a(\Omega, v_x, \theta) = \frac{1}{2}C_p(\lambda, \theta)\rho\pi R^2 v_x^3/\Omega. \tag{4}$$

The aerodynamic thrust force, which will be relevant for fatigue load reduction, can be modelled similar to the aerodynamic torque as

$$F_a(\Omega, v_x, \theta) = \frac{1}{2}C_t(\lambda, \theta)\rho\pi R^2 v_x^2. \tag{5}$$
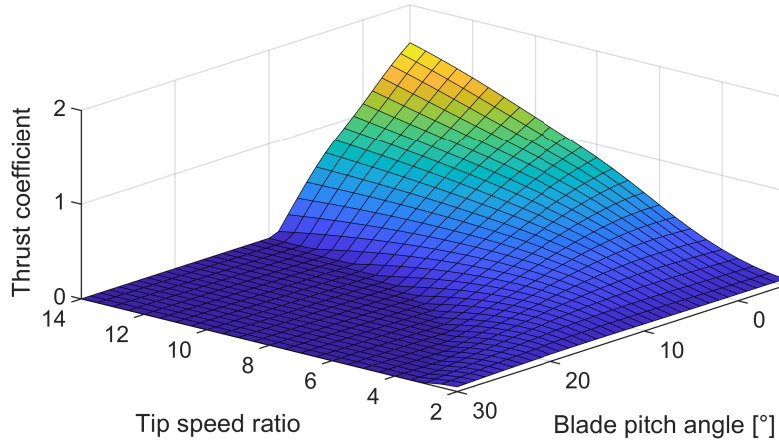
Figure 2. Thrust coefficient of the 15-MW reference turbine.

The thrust coefficient surface $C_t(\lambda, \theta)$ is shown in Figure 2. Notice that the thrust coefficient significantly decreases when the blade pitch angle becomes positive. For this reason, the largest thrust forces occur when switching between Regions 2 and 3.

In reality, wind is naturally turbulent, so the previous assumption of v_x as a uniform wind moving through the rotor disc is not accurate. Thus, we consider v_x to be the *rotor-effective wind speed* (REWS) of a turbulent wind field, which is the speed of a uniform wind field that causes the same aerodynamic torque (by (4)) as the turbulent wind field. It is a single wind speed value representing the equivalent horizontal and uniform upstream velocity.

2.2 Turbine low dimensional model

Based on Newton's second law of motion, the wind turbine is modelled by the following 1-dimensional nonlinear dynamical model:

$$J\dot{\Omega} = M_a(\Omega, v_x, \theta) - M_g. \tag{6}$$

Here $J = 318,628,138\,\mathrm{kg\,m^2}$ is the total moment of inertia of the rotating parts, including blades, hub, drivetrain, and generator, obtained from NREL (2021). The mechanical power extracted from the rotor by the generator is

$$P_{\mathrm{mech}} = \Omega M_g, \tag{7}$$

where M_g denotes the generator torque, and the electrical power is modelled as

$$P_{\mathrm{el}} = \eta_{\mathrm{gen}} P_{\mathrm{mech}}, \tag{8}$$

where η_{gen} is the generator efficiency, see Table 1. In order to produce the rated power of $15\,\mathrm{MW}$, a mechanical power of $15.536\,\mathrm{MW}$ is required.

2.3 Generator and blade pitch actuation

From (6)-(7), we see that the turbine power generation is determined by the rotor speed, and the rotor speed may be controlled by the generator torque and blade pitch angles. The generator torque is controlled via the power electronics in the generator (Gao et al., 2021). The power electronics response is significantly faster than the dynamics of the model (6), as is the blade pitch actuation. Thus, for control design purposes, we disregard these dynamics and treat both M_g and θ as control inputs that are immediately available for control actuation. In simulations we do assume blade pitch actuation dynamics, however; see Section 5 for details.

2.4 Control objective and operating points

In this section we detail the control objectives based on the model (6). The steady-state operating points for $\Omega, M_g, P_{\text{mech}}$ and θ as functions of the wind speed v_x are shown in Figure 3, and explained in the following. The rotor speed reference Ω_{ref} is to be kept between the minimum and maximum/rated speeds Ω_{min} and Ω_{rated} given in Table 1. The minimum value Ω_{min} avoids resonance with the tower. The reference Ω_{ref} follows the optimal tip speed ratio λ_{opt} whenever these constraints allow, leading to the formula

$$\Omega_{\text{ref}}(v_x) = \max\{\min\{\lambda_{\text{opt}}v_x/R, \Omega_{\text{rated}}\}, \Omega_{\text{min}}\}. \tag{9}$$

Below rated wind speed, the steady-state blade pitch angle θ_{ref} is such that the power coefficient is maximized for the current tip speed ratio; note that when the lower saturation Ω_{min} is active, the tip speed ratio is below λ_{opt}, and highest power coefficient is achieved for positive θ. Above rated wind speed, θ_{ref} is such that rated power is achieved, and hence given by the implicit equation

$$P_{\text{rated}}\eta_{\text{gen}}^{-1} = P_a(\Omega_{\text{rated}}, v_x, \theta_{\text{ref}}(v_x)). \tag{10}$$

The power curve in Figure 3 is the aerodynamic power achieved when rotor speed and blade pitch angle follow (9) and (10), i.e.

$$P_{\text{ref}}(v_x) = P_a(\Omega_{\text{ref}}(v_x), v_x, \theta_{\text{ref}}(v_x)). \tag{11}$$

The generator torque curve in Figure 3 is

$$M_{\text{g,ref}}(v_x) = P_{\text{ref}}(v_x)/\Omega_{\text{ref}}(v_x). \tag{12}$$

The main goal of the controller is to track these reference/steady-state values depending on the time-varying REWS v_x.

Peak shaving is a technique to reduce aerodynamic thrust force peaks by modifying θ_{ref} (Abbas et al., 2022). Figure 4 shows the original θ_{ref} and the incurred aerodynamic thrust force F_a, computed using (5), as dashed lines. Notice that a sharp peak occurs around rated rotor speed; this is because F_a is proportional to v_x^2, but significantly declines as θ increases, as can be seen in Figure 2. Peak shaving reduces this by already actuating blades slightly below rated wind speed. This comes at minimal
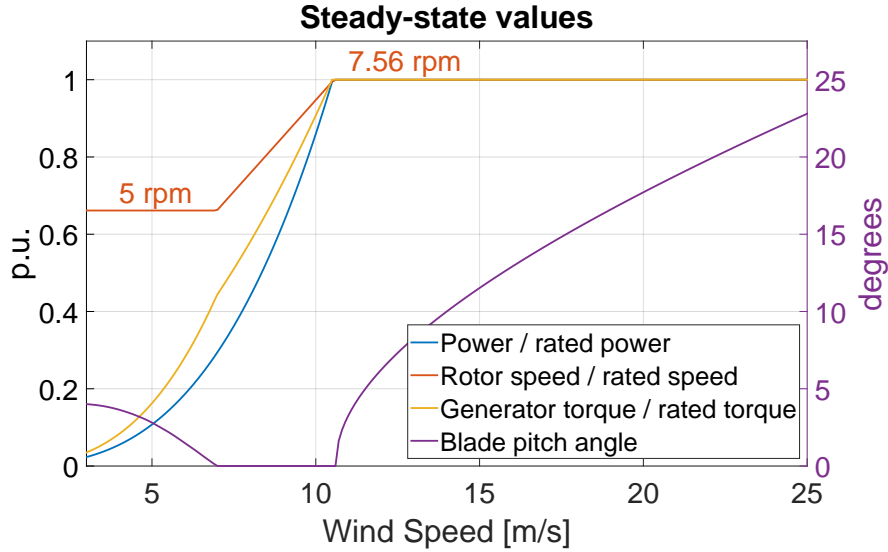
Figure 3. Desired equilibrium operating points of (6) without peak shaving.

power sacrifice thanks to the flatness of the C_p-surface (see Figure 1) at low θ. We limit F_a at 2 MN. This leads to a minimum pitch schedule $\theta_{\min}(v_x)$, which is obtained by solving

$$F_a(\Omega_{\mathrm{ref}}(v_x), v_x, \theta_{\min}(v_x)) = 2\,\mathrm{MN} \tag{13}$$

when a solution exists, and equal to the previously defined θ_{ref} otherwise. This $\theta_{\min}$, shown in Figure 5, acts as lower saturation for θ in all our considered controllers.

2.5 Fatigue loads

Wind turbulence leads to ever-changing stress and strain of the mechanical components, and ultimately material fatigue. Lowering these fatigue loads compared to state-of the art controllers is the main objective of the NOR controller proposed in this work. The four principal fatigue loads, illustrated in Figure 6, and the typical highest displacements that occur under normal operation of the IEA-15MW turbine, are:

1. tower fore-aft bending moment M_{yT}: In wind direction, caused by the aerodynamic thrust force of incoming wind, up to 1 m.

2. tower side-to-side bending moment M_{xT}: Sideways, caused by the aerodynamic torque transferred to the tower, up to 20 cm.

3. blade flapwise bending moment M_{yB}: In wind direction, caused by aerodynamic thrust force, up to 20 m.

4. Main shaft torsion (MST): Torsion of the shaft connecting the rotor with the generator, up to $0.005°$.
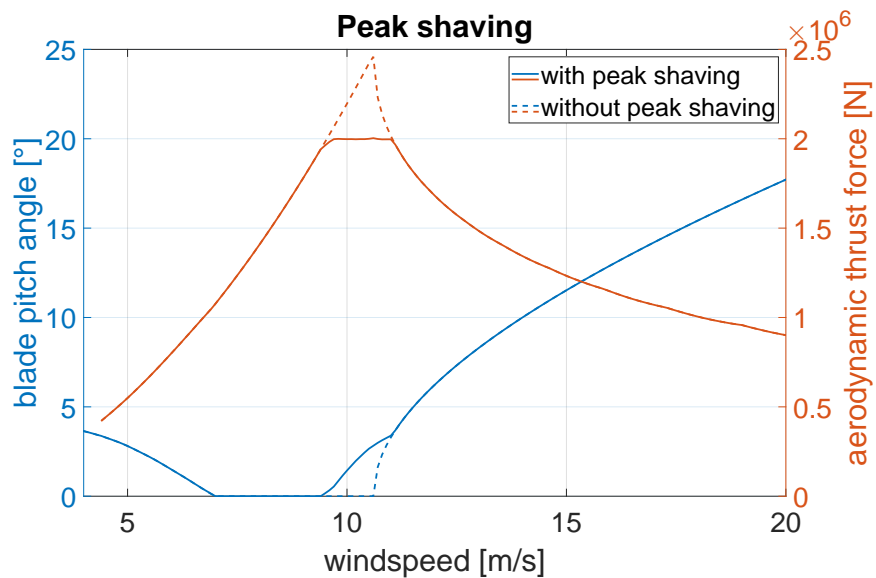
Figure 4. Blade pitch angles (blue) and aerodynamic thrust forces (red) with peak shaving (solid) and without (dashed). The dashed blade pitch angle is the same as in Figure 3.
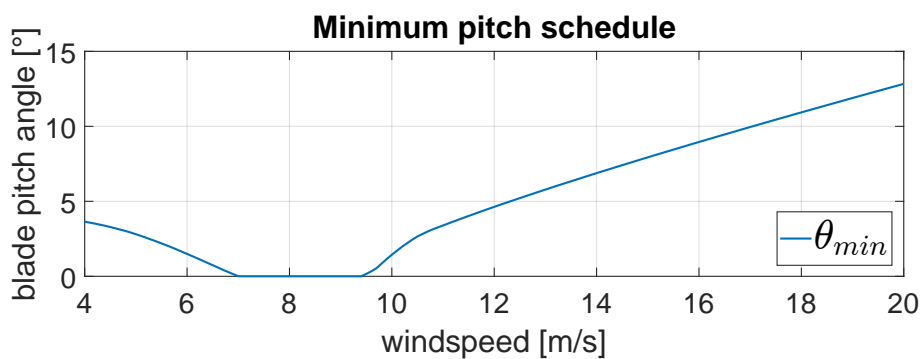
Figure 5. Minimum blade pitch angles to achieve optimal power coefficient at low wind speed, and limit aerodynamic thrust force at 2 MN at high wind speed by (13) with peak shaving.
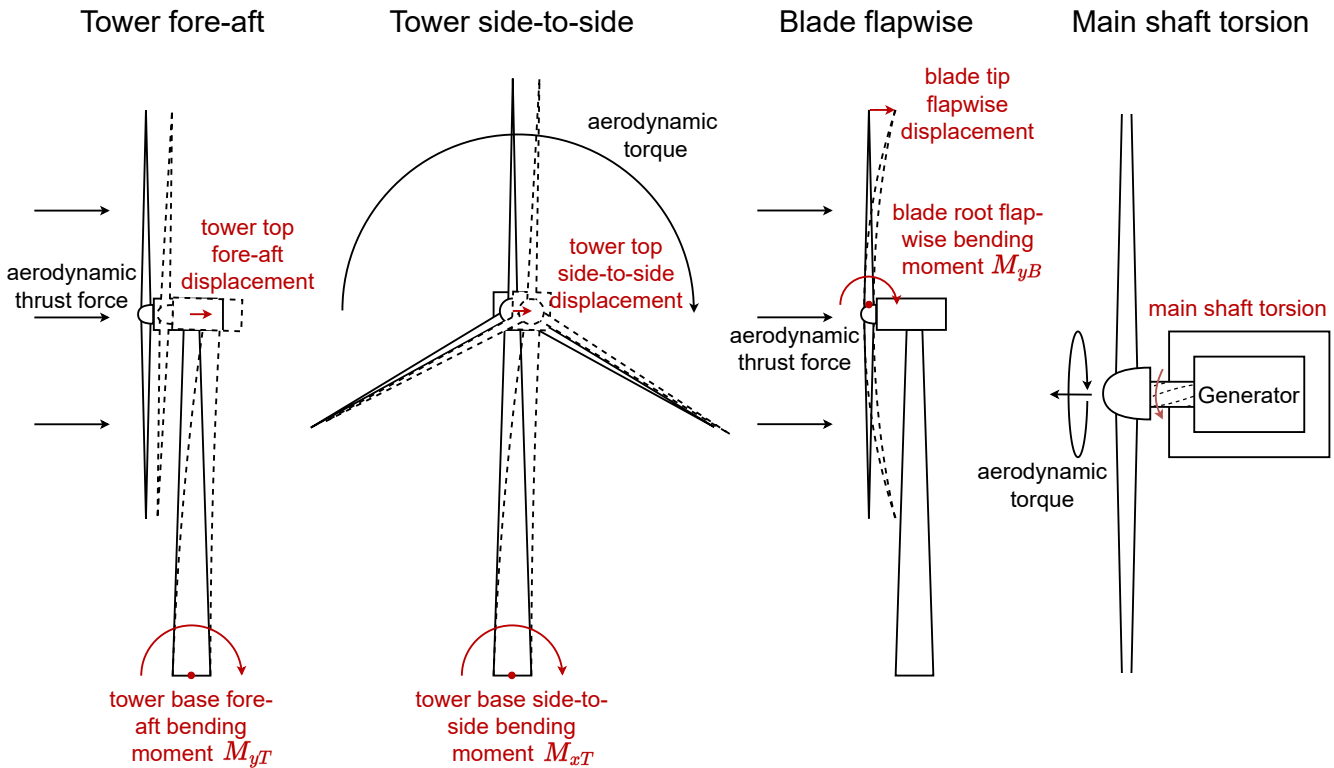
Figure 6. Visualizations of principal fatigue loads. Tower fore-aft and blade flapwise bending are mainly a result of aerodynamic thrust force, while tower side-to-side bending and main shaft torsion are mainly caused by aerodynamic torque.

The blade edgewise bending moment is another important fatigue load, but it is mostly due to the motion of the blades under gravity. As this cannot be alleviated by any control actuation, we will not consider it in our performance comparisons.

The bending, while being largely proportional to the aerodynamic thrust force for tower fore-aft and blade flapwise, or
195 generator torque for tower side-to-side and main shaft torsion, have additional natural oscillations, see Gaertner et al. (2020) for details. The oscillations are slightly dampened due to air and material resistance. The blade flapwise bending is also affected by the position of the blade within the rotor disc. This is because wind is typically stronger at higher altitude. Therefore the blades, if controlled with collective pitch control (which is the case for all controllers considered in this paper), bend more when they point upwards. This adds an oscillation in synchronicity with the rotor rotation.

200 **2.6   Fatigue load analysis**

To estimate the material fatigue, rainflow counting and Miner's rule are used to calculate a damage-equivalent load based on the root moments. As larger load cycles cause disproportionately greater damage, cycle amplitudes are weighted with the Wöhler

exponent and summed. The damage equivalent load (DEL) is calculated as

$$DEL = \left(\frac{T_{20\,\text{years}}}{T n_{\text{C,ref}}} \sum_{k=1}^{K} n_k A_k^m \right)^{1/m}, \tag{14}$$

where

1. $T_{20\,\text{years}} = 631134720\,\text{s}$ is the nominal lifespan of the turbine, 20 years,

2. $n_{\text{C,ref}} = 2 \times 10^6$ is a reference number of cycles, the value was chosen as in (Schlipf, 2016),

3. T is the time duration of the load history,

4. K is the number of rainflow cycles,

5. A_k is the amplitude of the kth cycle,

6. $n_k = 0.5$ or $n_k = 1$, depending on whether the kth cycle is a half cycle or full cycle,

7. m is the Wöhler exponent. Empirically found values of $m = 4$ for welded steel (tower material) and $m = 10$ for fibreglass (blade material) are customary (Schlipf, 2016).

The interpretation of (14) is that two million cycles with the DEL as amplitude cause the same damage as the recorded load history, if it is repeated over the nominal lifespan of 20 years.

DELs from simulations at different mean wind speeds are combined according to the Weibull distribution in Figure 7 to obtain a lifetime DEL estimate. This figure shows a histogram obtained from 10-minute-mean wind speeds measured in Bremerhaven, Germany in the winter of 2009 (Schlipf, 2016). The lifetime DEL is a mean of the DELs from the individual simulations, weighted with the probability from the Weibull distribution and the Wöhler exponent.

Due to the high Wöhler exponents, the material fatigue is mostly constituted of a few large cycles, rather than many small cycles. The highest peaks and lowest valleys have a large influence on the DEL. This means that the transition performance between Regions 2 and 3 is crucial, because that is where the highest aerodynamic thrust occurs, as noted in Section 2.5. Wind turbulence naturally leads to a lot of fluctuation in the bending. The aim of our controller design will be to reduce these fluctuations, while still generating maximum power. This will be achieved by smooth yet firm control action to make the peaks and valleys less extreme and avoid excitation of natural frequencies. This will require real-time wind speed estimation, which is discussed in the next section.

3   Wind speed estimation

In this section we discuss the two approaches to wind speed estimation that will be employed in our simulations. The first approach uses data available from the turbine's SCADA to compute the rotor effective wind speed (REWS). Many such model-based estimation techniques have been proposed in the wind energy research community. (Soltani et al., 2013) present

eawe
european academy of wind energy

WIND
ENERGY
SCIENCE
DISCUSSIONS
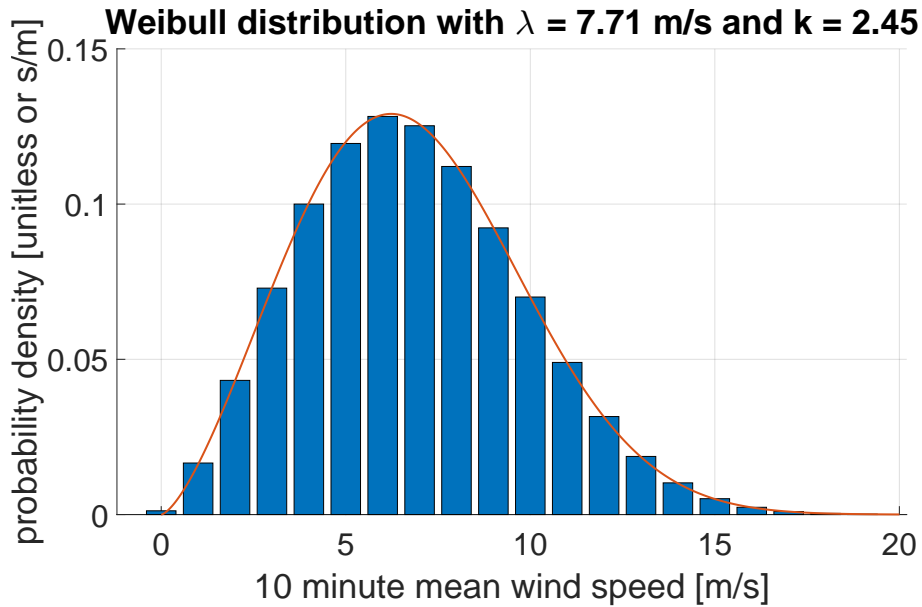
Figure 7. Weibull distribution adapted from (Schlipf, 2016, Figure 2.9) based on mean wind speeds recorded in Bremerhaven at a reference height of 102m, with scale parameter λ and shape parameter k.

a comprehensive list of REWS estimators until 2013, and compare them in simulations and field tests. There, the *Immersion and Invariance (I&I)* estimator was found to be among the best performance-wise, while being the simplest to implement. It was recently employed in (Woolcock et al., 2023).

Secondly we briefly describe wind speed estimation obtained from LIDAR measurements.

3.1 Immersion & Invariance estimator

Immersion and Invariance was first introduced in (Astolfi and Ortega, 2003) as a tool for stabilization and adaptive control of nonlinear systems, also see (Astolfi et al., 2008). In (Liu et al., 2009) these ideas were adapted for parameter identification of nonlinear systems. The premise here is that a nonlinear system depends on an unknown constant parameter. Based on monotonicity, the I&I estimator converges to that parameter. In (Ortega et al., 2011) and (Ortega et al., 2013) this technique was applied to wind speed estimation in wind turbines. The wind speed is naturally time-varying, but still treated like the constant unknown parameter. This is suitable, as long as the dynamics of the observer are significantly faster than changes of the REWS.

The general formulation of the I&I estimator based on (Ortega et al., 2013) is:

Proposition 3.1. *Consider the system*

$$\dot{x} = F(t) + \Phi(x, \xi) \tag{15}$$
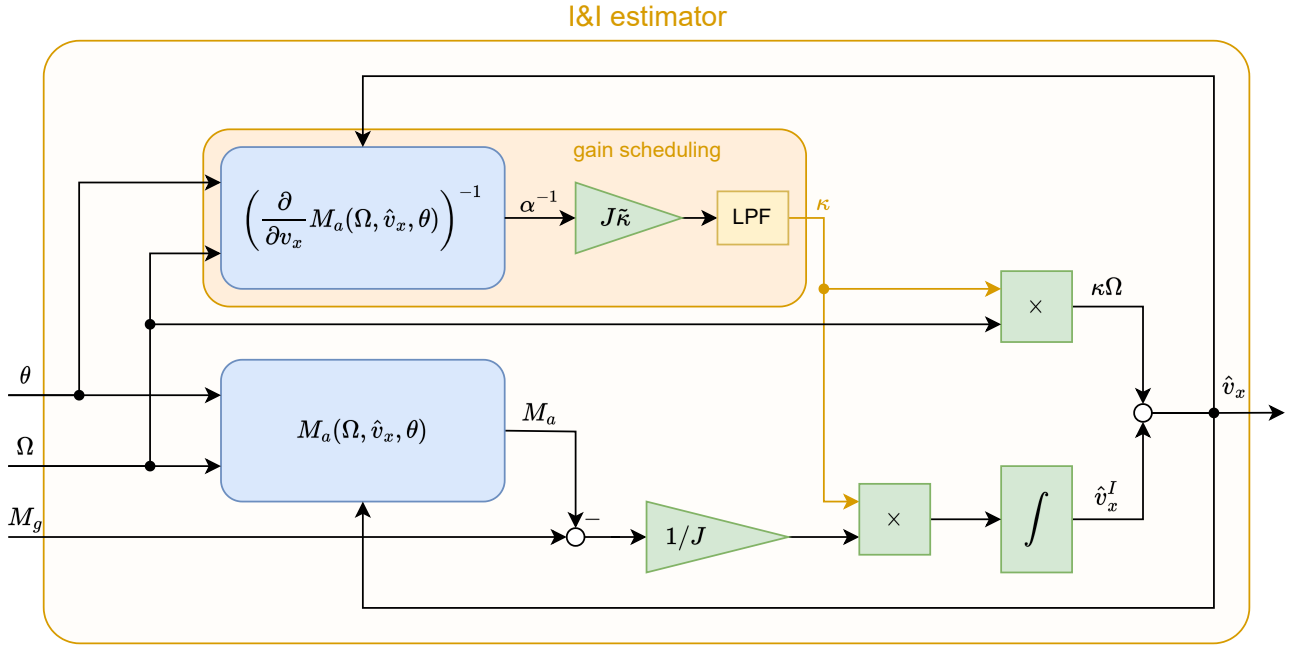
Figure 8. Overview of the I&I estimator based on (20) and (21), with gain scheduling described in Section 3.1.1. Inputs are the blade pitch angle θ, rotor speed Ω and generator torque M_g. The output is the wind speed estimate $\hat{v}_x$. Blue boxes mean that a (nonlinear) function is applied, where $M_a(\Omega, v_x, \theta)$ is the aerodynamic torque as in (4). Green triangles are gains, and $\times$ indicates multiplication of signals. LPF means low-pass filter.

where $x(t) \in \mathbb{R}$, the function $F(t)$ and the mapping $\Phi : \mathbb{R} \times \mathbb{R} \to \mathbb{R}$ are known, and $\xi \in \mathbb{R}$ is a constant unknown parameter. Assume that there exists a smooth mapping $\beta : \mathbb{R} \to \mathbb{R}$ such that the parametrized mapping

$$Q_x : \mathbb{R} \to \mathbb{R}, \quad \xi \mapsto \beta'(x)\Phi(x, \xi)$$

is strictly monotone increasing. Then the I&I estimator

$$\dot{\hat{\xi}}^I = -\beta'(x)\left(F(t) + \Phi\left(x, \hat{\xi}^I + \beta(x)\right)\right), \tag{16}$$

$$\hat{\xi} = \hat{\xi}^I + \beta(x) \tag{17}$$

is asymptotically consistent. That is,

$$\lim_{t \to \infty} \hat{\xi}(t) = \xi \tag{18}$$

for all $\left(x(0), \hat{\xi}^I(0)\right) \in \mathbb{R} \times \mathbb{R}$ and $F(t)$ such that $\left(x(t), \hat{\xi}(t)\right)$ exist for all $t \geq 0$.

In (Ortega et al., 2011) and (Ortega et al., 2013) the I&I estimator is applied to the wind turbine dynamics (6), except they only considered Region 2. The generalization to both Region 2 and 3 is immediate. The identification of variables in (15) is:

1. $x := \Omega$ is the rotor speed, $\xi := v_x$ is the rotor-effective wind speed, and $\hat{\xi} := \hat{v}_x$, $\hat{\xi}^I = \hat{v}_x^I$.

2. $F(t) := -M_g(t)/J$ is the acceleration of the rotor from the generator, and $\Phi(x,\xi) := M_a(\Omega, v_x, \theta)/J$ is the acceleration caused by aerodynamic torque.

3. $\beta(x) := \kappa x$ for a design parameter $\kappa > 0$.

A diagram of the I&I estimator is shown in Figure 9. To understand why the estimator works, consider the combined dynamics of the turbine and observer, which are

$$\dot{\Omega} = \frac{1}{J} M_a(\Omega, v_x, \theta) - \frac{1}{J} M_g, \tag{19}$$

$$\dot{\hat{v}}_x^I = \frac{\kappa}{J} \left(M_g - M_a(\Omega, \hat{v}_x, \theta) \right), \tag{20}$$

$$\hat{v}_x = \hat{v}_x^I + \kappa \Omega, \tag{21}$$

leading to

$$\dot{\hat{v}}_x = \dot{\hat{v}}_x^I + \kappa \dot{\Omega} = \frac{\kappa}{J} \left(M_a(\Omega, v_x, \theta) - M_a(\Omega, \hat{v}_x, \theta) \right). \tag{22}$$

Now the need for the monotonicity assumption becomes apparent: If, assuming constant Ω and θ, the function $M_a(\Omega, v_x, \theta)$ is strictly monotone increasing in v_x, then $\hat{v}_x$ converges to v_x. The term v_x^3 in the aerodynamic torque is monotone increasing. However, v_x also appears in M_a through the tip speed ratio and the power coefficient. For very high or low tip speed ratio the power coefficient drops rapidly, which can cause $M_a(\Omega, v_x, \theta)$ to decrease as v_x increases. In (Ortega et al., 2011) and (Ortega et al., 2013) sufficient conditions for monotonicity of the aerodynamic torque within a certain range are given. In all simulations conducted for this paper the I&I estimator was stable, indicating that under typical operating conditions the monotonicity is fulfilled.

3.1.1 Gain-scheduling of I&I estimator

Due to the nonlinearity of the aerodynamic torque, the I&I estimator with constant gain κ would have different time constants at different operating points. To counteract this, κ is adapted depending on the current wind speed estimate. Let $\tilde{\kappa}$ be the desired I&I cut-off frequency, and let

$$\alpha := \frac{\partial}{\partial v_x} M_a(\Omega, \hat{v}_x, \theta) \tag{23}$$

be the sensitivity of the aerodynamic torque with respect to wind speed at the current rotor speed, wind speed estimate and blade pitch angle. The unfiltered I&I gain is then

$$\kappa_{\text{unfiltered}} = \tilde{\kappa} J \alpha^{-1}. \tag{24}$$

This is passed through a low-pass filter (LPF) with long (slow) time constant to yield κ, in order to avoid harmful contributions of the gain-scheduling to the estimator dynamics.

3.2 LIDAR wind speed estimation

LIDAR uses infrared light and the Doppler effect to measure the horizontal wind speed v_x at a number of evenly distributed points on a circular cross-section of the wind field at the focal distance from the rotor plane (Schlipf et al., 2023). Spatial averaging is applied to the wind speeds at each point to estimate v_x at the focal distance from the turbine blades. See Schlipf (2016) for further information on the use of LIDAR in wind turbine control. The details of the LIDAR implementation in our simulations are given in Section 5.

4 Wind turbine control methodologies

In this section we describe the control methodologies that will be compared in our simulations. We first introduce the novel Nonlinear Output Regulation (NOR) controller and its combinations with I&I and LIDAR REWS estimators. Then we describe the ROSCO controller of Abbas et al. (2022), which will serve as the benchmark for performance comparisons, before comparing it to NOR+I&I from a conceptual perspective.

4.1 Nonlinear Output Regulation with I&I wind estimator

In this section a simple nonlinear wind turbine controller is proposed. The aim is to regulate the turbine rotor speed for Region 2 and 3 power generation, and hence we describe it as Nonlinear Output Regulation (NOR) control. The controller requires a REWS estimate $\hat{v}_x$, obtained from the I&I estimator, and hence we adopt the acronym NOR+I&I.

Figure 9 shows the closed-loop setup of NOR+I&I. Design is based on the 1-dimensional model for rotor speed dynamics (6), i.e.,

$$J\dot{\Omega} = M_a(\Omega, v_x, \theta) - M_g, \tag{25}$$

where M_g and θ are control inputs and v_x an exogenous disturbance. The rotor speed reference Ω_{ref} is similar to (9), but using the wind speed estimate $\hat{v}_x$ in place of the unknown v_x, i.e.,

$$\Omega_{\text{ref}} = \max\left(\min\left(\frac{\lambda_{\text{opt}}\hat{v}_x}{R}, \Omega_{\text{rated}}\right), \Omega_{\text{min}}\right). \tag{26}$$

The idea of the NOR controller is that, if $\hat{v}_x = v_x$, the rotor speed shall follow the desired closed loop dynamics

$$\dot{\Omega} = \mu(\Omega_{\text{ref}} - \Omega), \tag{27}$$

where $\mu > 0$ is a design parameter. Multiplying this with J and equating it with (25) leads to the equation

$$M_a(\Omega, v_x, \theta) - M_g = J\mu(\Omega_{\text{ref}} - \Omega), \tag{28}$$

which the controller must satisfy at all times. NOR now chooses θ and M_g depending on Ω and $\hat{v}_x$ such that (28) holds, the additional requirements specific to Regions 2 and 3 are satisfied, and that the transition between the regions is smooth.
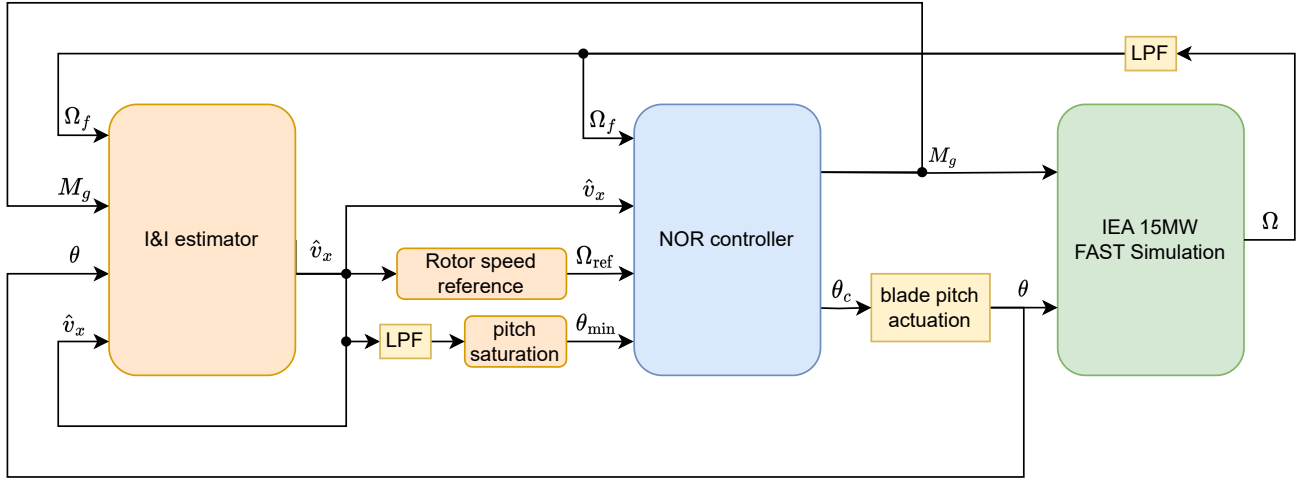
Figure 9. Overview of the NOR+I&I closed loop. Ω and Ω_f are unfiltered and filtered rotor speed, M_g is generator torque, θ_c is blade pitch control, θ is blade pitch angle after the actuation dynamics, and $\hat{v}_x$ is the wind speed estimate. See Figure 8 for the I&I estimator and Algorithm 1 for the NOR controller. The "Rotor speed reference" and "pitch saturation" blocks apply the functions Ω_{ref} in (26) and $\theta_{\min}$ in Figure 5, respectively. Yellow blocks are low-pass filters.

This leads to the control law given in Algorithm 1, which is further explained in the following. For this explanation we disregard the rotor speed low-pass filter and blade pitch actuation dynamics, i.e., assume $\Omega_f = \Omega$ and $\theta = \theta_c$.

The parameter $\varphi \in [0, 1]$ indicates whether the controller in Region 3 is designed to track rated torque, rated power or a combination of these. By (31), $\varphi = 1$ leads to constant torque $M_g = M_{\text{rated}}$, and $\varphi = 0$ leads to constant power by $M_g = P_{\text{rated}}/\Omega$. In all subsequent simulations $\varphi = 1$ is used. The minimum pitch schedule $\theta_{\min}$ is as in Figure 5.

This controller regulates rotor speed in Region 2 using the generator torque, by compensating aerodynamic torque and adding a feedback term based on the desired closed loop dynamics (see (30), note the similarity to (28)). If this generator torque control (30) were to exceed rated torque (if $\varphi = 1$) or rated power (if $\varphi = 0$), i.e. the inequality in the if-condition is not satisfied, then the else-branch representing the Region 3 control applies. Then, equation (32) always has a unique solution θ that is at least $\theta_{\min}(\hat{v}_x)$, because $M_a(\Omega, \hat{v}_x, \theta_{\min}(\hat{v}_x)) - M_g > J\mu(\Omega_{\text{ref}} - \Omega)$, and $M_a(\Omega, \hat{v}_x, \theta)$ is continuous and monotone decreasing in θ for $\theta \geq \theta_{\min}(\hat{v}_x)$. By substituting in θ and M_g (from either region) into (25), it can be seen that the closed loop always follows (27), if the wind speed estimate is perfectly accurate, i.e. $\hat{v}_x = v_x$, as intended.

Furthermore, the controller performs a smooth transition between Regions 2 and 3, meaning that θ and M_g do not jump. Indeed, at the time of region switching it holds that

$$M_a(\Omega, \hat{v}_x, \theta_{\min}(\hat{v}_x)) + J\mu(\Omega - \Omega_{\text{ref}}) = \varphi M_{\text{rated}} + (1 - \varphi)\frac{P_{\text{rated}}}{\Omega}, \tag{33}$$

Algorithm 1 Nonlinear output regulation (NOR) controller

Inputs: wind speed estimate $\hat{v}_x$, low-pass filtered rotor speed Ω_f

Outputs: generator torque M_g, blade pitch angle control θ_c

if $M_a(\Omega_f, \hat{v}_x, \theta_{\min}(\hat{v}_x)) + J\mu(\Omega_f - \Omega_{\text{ref}}) \leq \varphi M_{\text{rated}} + \frac{(1-\varphi)P_{\text{rated}}}{\Omega_f}$ **then**

    (Region 2 / below-rated operation)

$$\theta_c \leftarrow \theta_{\min}(\hat{v}_x) \tag{29}$$

$$M_g \leftarrow M_a(\Omega_f, \hat{v}_x, \theta_{\min}(\hat{v}_x)) + J\mu(\Omega_f - \Omega_{\text{ref}}) \tag{30}$$

else

    (Region 3 / above-rated operation)

$$M_g \leftarrow \varphi M_{\text{rated}} + (1-\varphi)\frac{P_{\text{rated}}}{\Omega_f} \tag{31}$$

    solve $M_g = M_a(\Omega_f, \hat{v}_x, \theta_c) + J\mu(\Omega_f - \Omega_{\text{ref}})$ for θ_c (32)

end if

---

under the assumption that all the signals are continuous. The torque controls (30) and (31) in Regions 2 and 3 are the left and
325   right-hand side of that equation and therefore coincide. Furthermore, the solution of (32) is then $\theta_{\min}(\hat{v}_x)$, and indeed equal to
(29).

NOR+I&I compensates model errors in the C_p-surface (that NOR heavily relies upon) without the need of an integrator.
This is detailed in Appendix A.

4.2   Nonlinear Output Regulation with I&I and LIDAR

330   NOR+I&I can be improved by adding LIDAR wind preview information, for which we use the acronym NOR+I&I+LIDAR.
We propose to use a weighted average of LIDAR and I&I. This has performed better than just LIDAR in our simulations. The
reasons are twofold, namely,

    1. the LIDAR signal is a look-ahead estimate, while the I&I estimate, which can be seen as a low-pass filtered REWS, lags
       behind. By averaging the two, we obtain a more accurate real-time estimate of the current wind speed at the rotor.

335   2. High frequency fluctuations of the LIDAR and I&I signals are mostly independent of each other. Therefore, the average
       has a lower variation than the individual signals. This leads to smoother control action, which in turn reduces fatigue
       loads (as discussed in Section 2.6) and actuator usage.

    Figure 10 shows an overview of the proposed application of LIDAR. Firstly, a mean correction is applied to the LIDAR
signal. This is because otherwise our simulations lead to a significant error between average Region 3 power generation and
340   rated power (note that this does not happen for NOR+I&I and the mean-corrected NOR+I&I+LIDAR because of the robustness
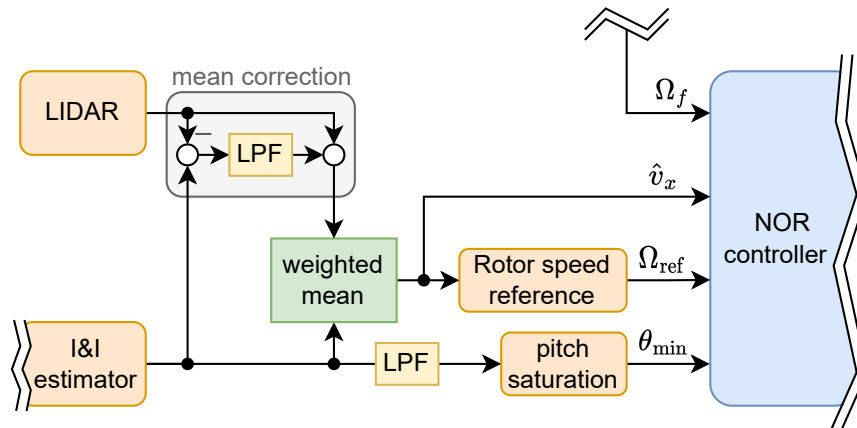
Figure 10. Section of Figure 9, with the addition of LIDAR.

explained in Appendix A). The mean correction subtracts the LIDAR signal from the I&I output, passes it through a low-pass filter, and adds this filtered difference back to the LIDAR signal. The resulting signal has the low-frequency content of the I&I estimate and high-frequency content of the LIDAR estimate. The time constant of the low-pass filter should be chosen to be more than a minute.

345   The unified I&I and LIDAR wind speed estimate serves as the input for the NOR controller as well as for the rotor speed reference generation. For the rest of this paper only the I&I estimate is used for minimum pitch saturation. This is for the sake of comparison with controllers not using LIDAR. Nevertheless, the LIDAR estimate could be used to improve peak shaving. For example, the maximum of LIDAR and I&I estimates could dictate minimum blade pitch angles. This would lead to reduced tower fore-aft and blade flapwise DELs: Peak shaving based on the delayed I&I estimate predominantly reduces rotor thrust

350   peaks from Region 3 to Region 2 switches. Peak shaving based on the leading LIDAR estimate reduces peaks from Region 2 to Region 3 switches. The combination of both reduces both kinds of peaks quite well. This comes at the cost of a slight power sacrifice, however.

4.3   Reference Open-Source baseline controller (ROSCO)

To compare the performance of the NOR controller, we shall use ROSCO, the state-of-the-art modular reference wind turbine

355   controller that was shown to perform comparably to, or better than, previous reference controllers in (Abbas et al., 2022). Figure 11 shows an overview of the ROSCO setup used in this paper. The components are explained in the following, see Section 5 for tuning.

Wind speed estimator. A REWS estimate is used to determine rotor speed reference and minimum blade pitch angles. By default, ROSCO uses an Extended Kalman Filter (EKF). We replaced this by the I&I estimator for multiple reasons: The EKF

360   failed to be stable in our simulations, the I&I estimator is simpler, and for the sake of comparison between NOR+I&I(+LIDAR)
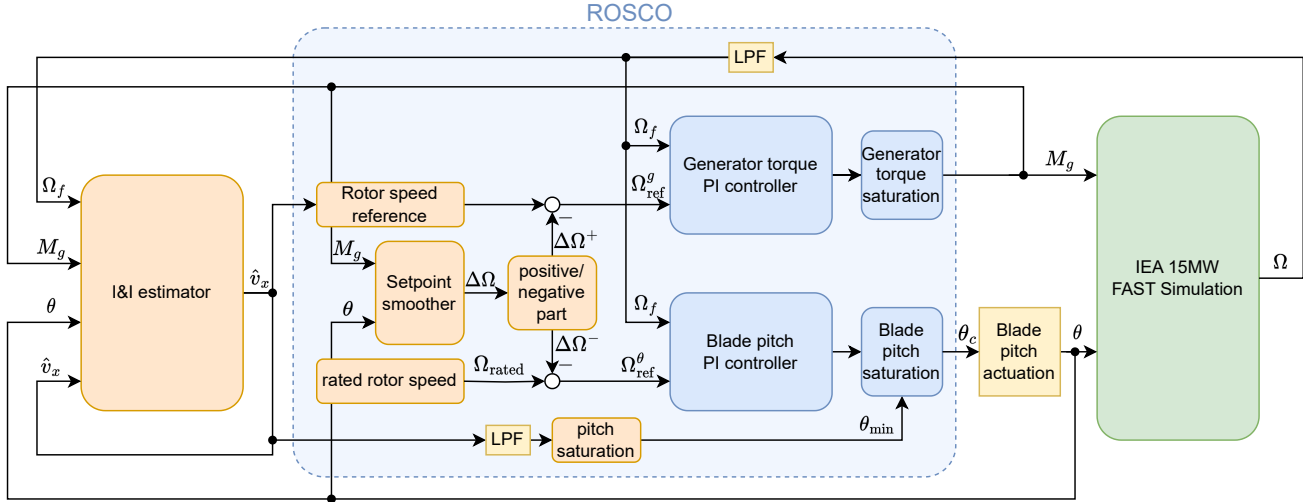
Figure 11. Overview of ROSCO simulation setup. The REWS estimate from the I&I estimator determines rotor speed reference and minimum blade pitch angles, as in NOR+I&I. Rotor speed regulation is achieved by two SISO PI controllers, where saturations and set point smoothing avoid conflict between them.

and ROSCO. Note that ROSCO uses the wind speed estimate only to generate the reference and for pitch saturation with $\theta_{\min}$, but not directly for rotor speed regulation. Therefore the choice of estimator has little impact on ROSCO's performance.

Torque and blade pitch PI controllers. For the generator torque and blade pitch angle controls, independent single-input single-output PI controllers, i.e.

$$M_g = K_P^g(\Omega_{\text{ref}}^g - \Omega_f) + K_I^g \int (\Omega_{\text{ref}}^g - \Omega_f) \, \mathrm{d}t, \tag{34}$$

$$\theta_c = K_P^\theta(\Omega_{\text{ref}}^\theta - \Omega_f) + K_I^\theta \int (\Omega_{\text{ref}}^\theta - \Omega_f) \, \mathrm{d}t, \tag{35}$$

are used. To account for nonlinearity of the aerodynamic torque, the blade pitch controller is gain-scheduled. Details on that can be found in Section B. The generator torque control is saturated at rated torque (this usually occurs in Region 3). The blade pitch angle control is saturated to be at least a certain minimum blade pitch angle (this usually occurs in Region 2 and around rated wind speed), details are further below.

Reference signal and set point smoothing. The rotor speed reference Ω_{ref}^g for the generator torque controller is based on (9), i.e., optimal tip speed ratio saturated between minimum and rated rotor speed. The rotor speed reference $\Omega_{\text{ref}}^\theta$ for the blade pitch controller is based on rated rotor speed. In order to ensure proper region switching, these values are modified by a set point smoothing technique. A correction term

$$\Delta\Omega = \left[\left(\frac{\theta - \theta_{\min}}{\theta_{\max}} \right) k_{\text{vs}} - \left(\frac{M_{\text{g,rated}} - M_g}{M_{\text{g,rated}}} \right) k_{\text{pc}} \right] \Omega_{\text{rated}} \tag{36}$$

with design parameters k_{vs} and k_{pc} is computed. If it is positive, it is subtracted from the torque control reference, and if negative, subtracted from the pitch control reference instead. In view of Figure 11,

$$\Delta\Omega^+ = \max\{\Delta\Omega, 0\}, \quad \Omega^g_{\mathrm{ref}} = \Omega_{\mathrm{ref}} - \Delta\Omega^+,$$
$$\Delta\Omega^- = \min\{\Delta\Omega, 0\}, \quad \Omega^\theta_{\mathrm{ref}} = \Omega_{\mathrm{rated}} - \Delta\Omega^-.$$

380 Set point smoothing ensures, that most of the time one of the controllers is saturated: In Region 3, $\Delta\Omega$ is generally positive due to the blade pitch angles. Then, if $\Omega_f < \Omega_{\mathrm{rated}} = \Omega_{\mathrm{ref}}$, the set point smoothing still ensures that $\Omega^g_{\mathrm{ref}} < \Omega_f$, which makes the generator torque stay at rated, therefore not sacrificing power while the blade pitch control regulates rotor speed. Similarly, in Region 2 set-point smoothing ensures that blade pitch angles are generally equal to $\theta_{\min}$.

Pitch saturation. The pitch saturation by $\theta_{\min}$ (see Figure 5) serves two purposes: Power maximization at low wind speeds 385 as outlined in Section 2.4, and peak shaving.

Additional filters. Generator speed, as well as the wind speed estimate going into the pitch saturation, are low-pass filtered, in order to lessen the effect of measurement errors and reduce control actuation.

4.4 Comparison between NOR+I&I and ROSCO

We briefly compare NOR+I&I and ROSCO from a conceptual point of view. Note that NOR+I&I, even though it uses $\hat{v}_x$ 390 as feedforward, is still a feedback controller (like ROSCO), because the I&I estimator computes $\hat{v}_x$ from plant outputs. In theory, the first order plant dynamics (25), NOR (which uses a static control law with no internal states) and the first order I&I dynamics (22) lead to a second-order closed-loop, similar to the second-order dynamics that ROSCO is designed for. In Appendix B we provide a theoretical comparison between these two closed loops via linearization. This enables conversion of the tuning choices for the design parameters, in particular the proportional and integral gains of ROSCO to μ and $\tilde{\kappa}$ of 395 NOR+I&I and conversely. We use this procedure to tune NOR+I&I based on ROSCO's tuning, see Section 5 for details. This analysis identifying the linearized closed loops only works in Regions 2 and Region 3 in isolation, and does not take into account the region switching. Here lies one of the differences between NOR and ROSCO; while ROSCO employs set-point smoothing to avoid harmful interference between its two SISO loops, NOR by design transitions seamlessly between the regions. Furthermore, NOR permits direct inclusion of peak shaving into the control design, whereas ROSCO applies it as a 400 saturation after the blade pitch controller.

5 Turbine Simulation Environment and Tuning

Here we describe the various components of our simulation environment for testing the performance of the ROSCO and NOR controllers.

Turbine and wind simulation. We used openFAST (NREL, 2019) as our turbine simulator on the IEA 15-MW reference 405 turbine (Gaertner et al., 2020). Full-field wind signals of length 120 minutes with mean wind speeds between 5 and $20\,\mathrm{m\,s^{-1}}$ (at hub height) were generated with TurbSim using the parameters in Table 2. TurbSim generates realistic full-field wind signals

Duration	2 h
Turbulence class	B
Turbulence model	IECKAI
Power law exponent	default
Time step	0.25 s
number of grid points in vertical direction	33
number of grid points in horizontal direction	33
hub height	150 m
grid height	250 m
grid width	250 m

Table 2. TurbSim parameters

according to Taylor's frozen wind hypothesis, which models the wind field as a turbulence box moving towards the wind turbine at its mean wind speed. Based on a statistical model, TurbSim numerically simulates a time series of three-component wind speed vectors on a grid in a vertical plane. The time series is generated with inverse Fourier transform of the frequency
410   spectrum of velocity components and spatial coherence.

LIDAR simulation. We employed the simulation toolbox given in Schlipf et al. (2023) for the Molas NL400 LIDAR system with a focal distance of 240 m and 4 measuring points. As we adopted Taylor's frozen wind hypothesis, the wind field was assumed not to evolve between the focal point and the blades, and hence the wind evolution component of the toolbox was not used. This hypothesis is appropriate for relatively flat terrain where geological features do not interact with the air flow
415   between the measurement point and blades. To smoothen the signal for control purposes, the raw measurements are passed through a low-pass filter with cutoff frequency $0.1194 \, \mathrm{rad \, s^{-1}}$.

While it is common to buffer the filtered LIDAR signal with a time delay to synchronize it with the wind at the rotor (Schlipf et al., 2023), we do not do this in our study of NOR+I&I+LIDAR. This is done to fully take advantage of the fact that LIDAR is a look-ahead estimate for the combination with the lagging-behind I&I estimate, as discussed in Section 4.2.

420   **ROSCO implementation.** ROSCO is applied with peak-shaving and set point smoothing using the default parameters for the IEA 15MW reference turbine, shown in Table 3. As mentioned in Section 4.3, the ROSCO's EKF is replaced by the I&I estimator with same tuning as NOR+I&I.

NOR tuning. We choose $\tilde{\kappa}$ and η depending on mean wind speed. The NOR controller is tuned based on the tuning choices of ROSCO according to equations (B19) and (B20), which results in NOR+I&I and ROSCO having the same linearized closed
425   loop dynamics. This gives to $\tilde{\kappa} = \eta = 0.12 \, \mathrm{s^{-1}}$ for below-rated mean wind speed, and $\tilde{\kappa} = \eta = 0.2 \, \mathrm{s^{-1}}$ above rated. However, because the lower parameters performed better for NOR near rated wind speed, we only gradually increase $\tilde{\kappa}$ and η from $0.12 \, \mathrm{s^{-1}}$ to $0.2 \, \mathrm{s^{-1}}$, with the full $0.2 \, \mathrm{s^{-1}}$ at $14.59 \, \mathrm{m \, s^{-1}}$ above rated wind speed. Peak shaving is built into the NOR controller as outlined in Section 4.1.

Variable speed closed-loop frequency ω_{des}^g	$0.12\,\text{rad}\,\text{s}^{-1}$
Variable speed closed-loop damping ζ_{des}^g	1
Pitch control closed-loop frequency $\omega_{\text{des}}^\theta$	$0.2\,\text{rad}\,\text{s}^{-1}$
Pitch control closed-loop damping $\zeta_{\text{des}}^\theta$	1
Set point smoothing variable speed gain k_{vs}	1
Set point smoothing pitch control gain k_{pc}	10^{-3}
Set point smoothing max. blade pitch angle θ_{max}	$30°$

Table 3. ROSCO design parameters

Generator speed 2$^{\text{nd}}$-order LPF frequency	$1.008\,\text{rad}\,\text{s}^{-1}$
Generator speed 2$^{\text{nd}}$-order LPF damping	0.7
Wind speed 1$^{\text{st}}$-order LPF for pitch saturation	$0.21\,\text{rad}\,\text{s}^{-1}$
I&I variable gain 1$^{\text{st}}$-order LPF	$0.033\,\text{rad}\,\text{s}^{-1}$

Table 4. Additional low-pass filter parameters. The frequencies refer to the -3dB cutoff frequencies.

Additional filters. To model blade pitch actuation, a second order low-pass filter with undamped natural frequency $2\pi\,\text{rad}\,\text{s}^{-1}$
and damping factor 0.7 is included between the blade pitch angle output of the controllers and the blade pitch angle input of
openFAST. The following low-pass filters, as indicated in Figure 9, and with parameters given in Table 4, are used: In ROSCO,
the rotor speed measurement is by default passed through a second-order low-pass filter. The wind speed estimate, that minimum blade pitch angles are computed with, is passed through a first-order low-pass filter. For the sake of comparability, the
same filters are used for NOR+I&I. Finally, the variable gain of the gain-scheduled I&I estimator is filtered with a first-order
low-pass filter, to avoid harmful effects of the gain-scheduling on the dynamics. This applies for the I&I estimators in ROSCO
as well as NOR+I&I(+LIDAR).

Performance metrics. For each controller and each of the 16 mean wind speeds, eight performance metrics are computed
as follows from simulation data in the time interval between $t_{\text{start}} = 300\,\text{s}$ and $t_{\text{end}} = 7200\,\text{s}$:

– The average power generation,

– four metrics relating to the turbine fatigue loads, which are the tower fore-aft and side-to-side DELs based on root
moments, with Wöhler exponent 4; the average of the three blade flapwise DELs based on root moments, with Wöhler
exponent 10, and the main shaft torsion DEL based on rotor torque, with Wöhler exponent 4.

– Three metrics relating to the turbine operation, actuator usage and tracking performance: the average pitch rate,

$$\frac{1}{t_{\text{end}} - t_{\text{start}}} \int_{t_{\text{start}}}^{t_{\text{end}}} |\dot{\theta}(t)|\,\mathrm{d}t,$$

the RMS error between rotor speed $\Omega(t)$ and reference rotor speed (9),

$$\frac{1}{t_{\text{end}} - t_{\text{start}}} \sqrt{\int_{t_{\text{start}}}^{t_{\text{end}}} (\Omega(t) - \Omega_{\text{ref}}(\hat{v}_x(t)))^2 \, \mathrm{d}t,}$$

and the maximum rotor speed,

$$\max_{t_{\text{start}} \leq t \leq t_{\text{end}}} \Omega(t).$$

With the exception of the average power generation, a smaller measure indicates superior performance in all cases.

For the DELs, we computed weighted means across all wind speeds according to Wöhler exponent and a Weibull distribution
445   as described in Section 2.6. Because the Weibull distribution in Figure 7 models wind speeds at a reference height of 102m, we scale up the distribution according to the power law with exponent 0.2 to a reference height of 150m, resulting in a new shape parameter of $8.33\,\mathrm{m\,s^{-1}}$. For average power and pitch rate we calculate the arithmetic mean weighted with Weibull distribution, for RMS error the quadratic mean weighted with Weibull distribution, and for maximum rotor speed the maximum across all wind speeds.

450   6   Performance results and comparisons

The results of our turbine simulations comparing ROSCO, NOR+I&I and NOR+I&I+LIDAR are shown for individual mean wind speeds in Figure 12 and averaged across all wind speeds in Table 5. Time series of all three controllers at $10\,\mathrm{m\,s^{-1}}$ mean wind speed can be found in Figure 13.

Regarding NOR+I&I+LIDAR, we tested different weightings of the two REWS estimates, and found that an equal weighting
455   of 50% each generally performs best. Figure 13(c) shows both the I&I and LIDAR REWS estimates, with LIDAR being visibly ahead. High frequency contents of the signals are indeed fairly independent, supporting the idea that the average has less variation.

The tower fore-aft DELs were fairly close for all the three controllers, with the NOR controllers showing small improvements around rated wind speed. The NOR controllers also reduce side-to-side DELs; note that this data is less reliable, however, even
460   on 2 hour simulations, due to the small damping of the side-to-side bending. While NOR+I&I slightly worsens blade flapwise DEL, NOR+I&I+LIDAR yields significant improvements at high wind speeds. Fatigue loads at high wind speeds, despite their rarity, have a large impact on the the lifetime DEL due to the high Wöhler exponent of 10. This results in a 4.9% improvement in DEL, which corresponds to a 65% lifespan increase according to (14). The NOR controllers also reduce main shaft DEL and pitch rate. NOR+I&I+LIDAR in particular lowers pitch rate significantly by 22.62%. This confirms the idea that the lower
465   variation averaged estimate leads to lower actuator usage. NOR+I&I+LIDAR also slightly improves power capture near rated wind speed. Finally, NOR controllers improve overall tracking performance, indicated by the reduction in rotor speed RMS error and maximum rotor speed in Table 5. ROSCO's high rotor speed RMS error at low wind speeds is because, even though it is designed to track the minimum rotor speed of $5\,\mathrm{rpm}$, it typically yields lower rotor speed on average.

	ROSCO	NOR+I&I *cf.* ROSCO	NOR with half I&I, half LIDAR *cf.* ROSCO
Tower fore-aft DEL	`449.069 MNm`	−2.03%	−2.61%
Tower side-to-side DEL	`337.827 MNm`	−13.94%	−11.59%
Blade flapwise DEL	`49.133 MNm`	+0.81%	−4.72%
Main shaft torque DEL	`8.120 MNm`	−6.66%	−15.25%
Pitch rate	`0.027 °/s`	−6.06%	−22.62%
Average power	`7.587 MW`	−0.10%	+0.33%
Rotor speed RMS error	`0.483 rpm`	−38.07%	−37.19%
Maximum rotor speed	`9.124 rpm`	−0.88%	−0.32%

Table 5. Lifetime average performance metrics of ROSCO, and percentage change of NOR controllers compared to ROSCO. At the exception of average power, a reduction is always better.

Some further comparisons of the ROSCO and the NOR controllers from a systems theory perspective are included in the
470 Appendices.

7 Conclusions

We have introduced a novel nonlinear controller design methodology for wind turbine control that utilises wind speed estimation that may be derived from the turbine's SCADA, LIDAR measurements, or both. Extensive simulation studies over a broad range of mean wind speeds and performance metrics showed that the NOR controllers are always able to match the per-
475 formance of the state-of-the-art ROSCO baseline controller, and were able to improve upon it in several important DELs and turbine control measures. The best performance was obtained by using an average of the REWS and LIDAR wind estimates.

From a design perspective, NOR has several advantages over ROSCO. It utilises a simple nonlinear turbine model, and hence avoids the need for gain-scheduling methods based on a range of linearisation points. It provides a unified design approach over both operating regions. The closed loop maintains the desired dynamics, and Region 2 torque and Region 3
480 pitch controller transition in a continuous fashion. In this respect, NOR is also an improvement over the earlier gain-scheduled linear output regulation methods used in (Mahdizadeh et al., 2021) and (Woolcock et al., 2023). NOR enables direct inclusion of LIDAR wind speed estimates across operating regions, which ROSCO cannot do as easily. This enables the NOR+I&I+LIDAR controller, which showed significant performance improvements.

Further work can be done to tune NOR+I&I+LIDAR. The LIDAR signal could be buffered with a time delay that is carefully
485 chosen based on wind speed and the I&I time constant, such that the averaged signal is accurately aligned with wind speed at the rotor. This could significantly improve tracking performance and further reduce DELs. While in this work the NOR controller was designed to achieve maximum power point tracking, the controller can be adapted to output a different desired power. Thus future work can consider an application of NOR to problems of active power generation to provide grid frequency support services.
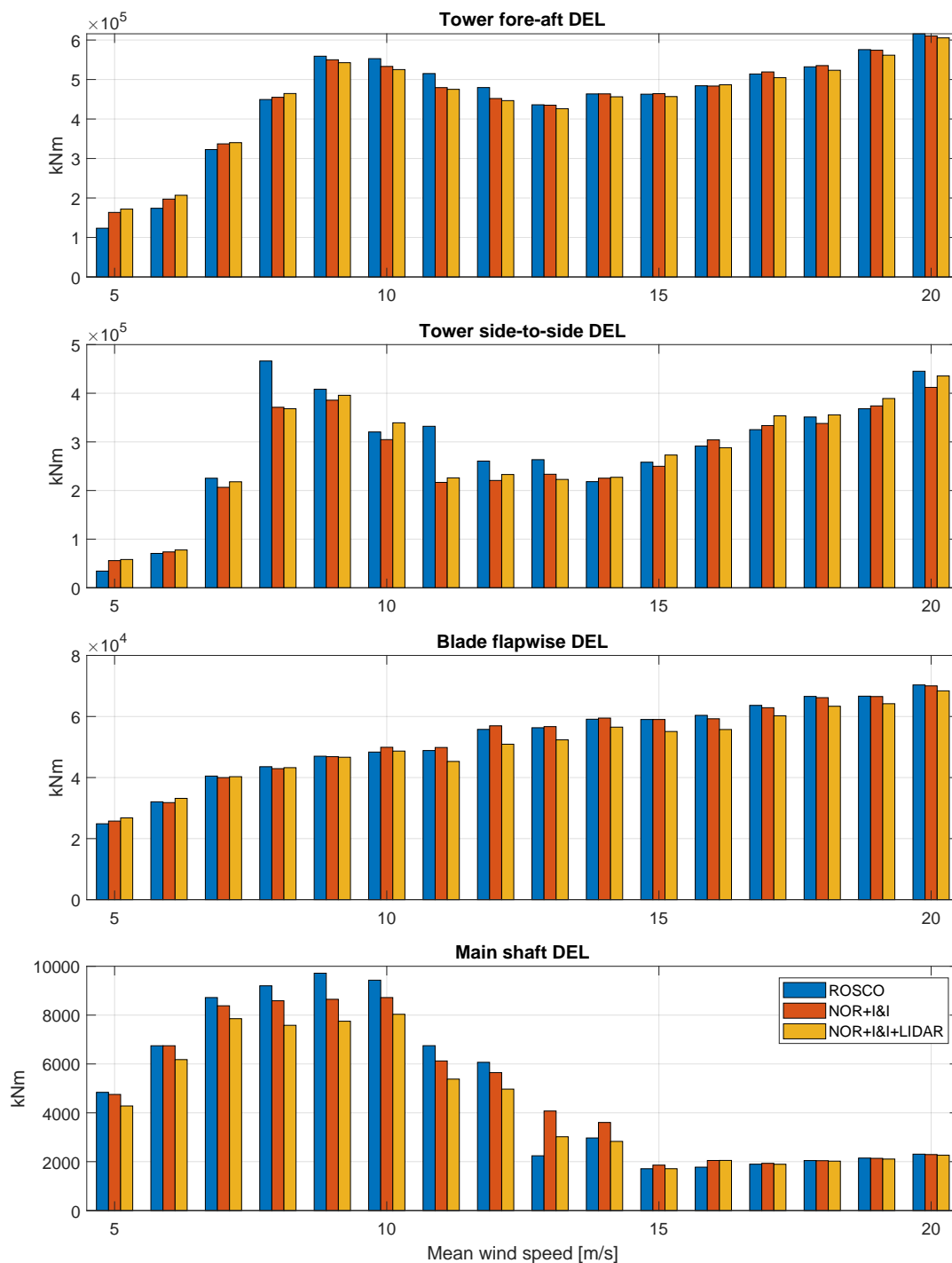
Figure 12. (a) Performance comparisons between ROSCO and NOR from 2 hour simulations at each wind speed on the IEA 15-MW turbine.
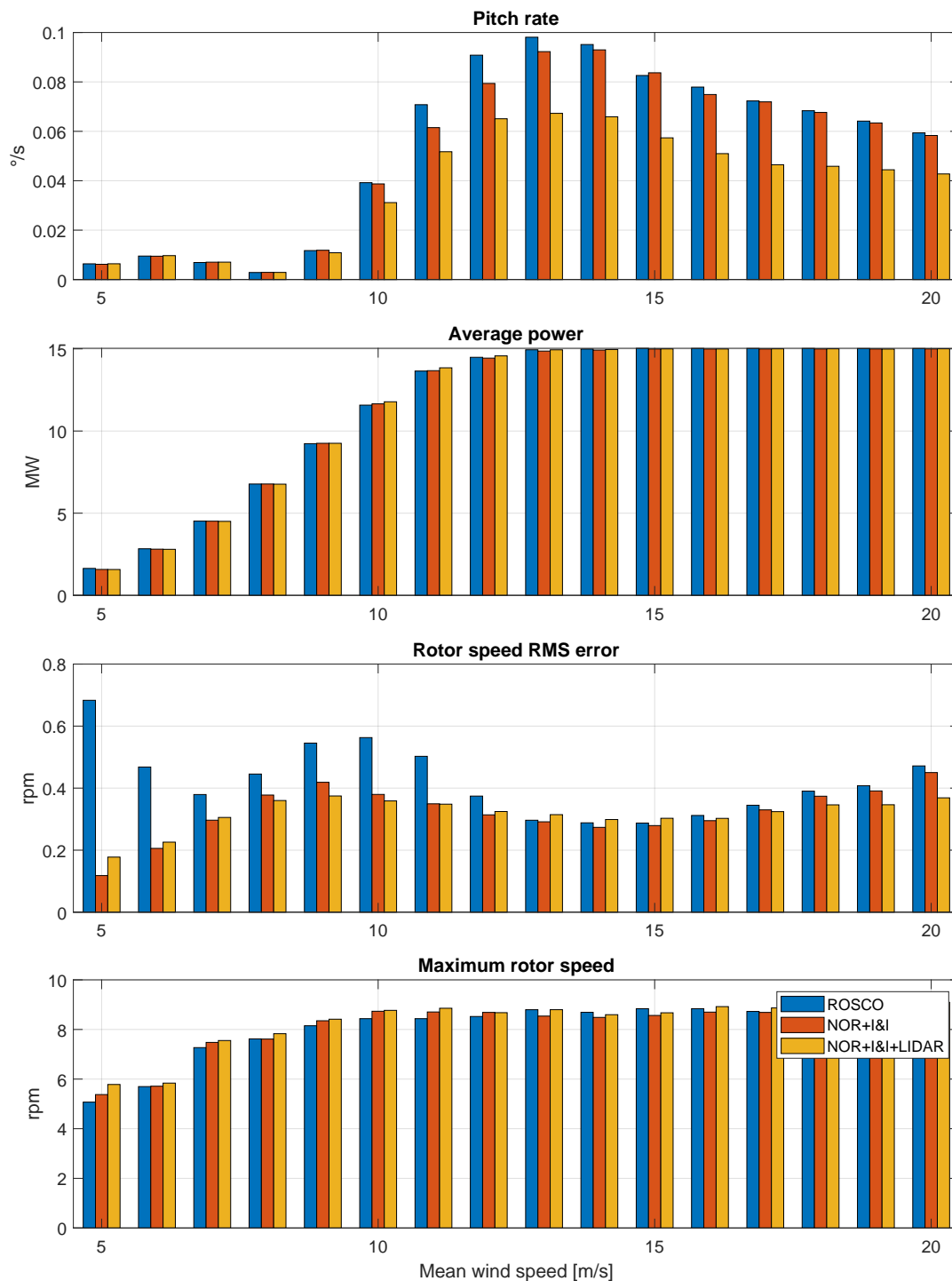
Figure 12. (b) Performance comparisons between ROSCO and NOR from 2 hour simulations at each wind speed on the IEA 15-MW turbine.
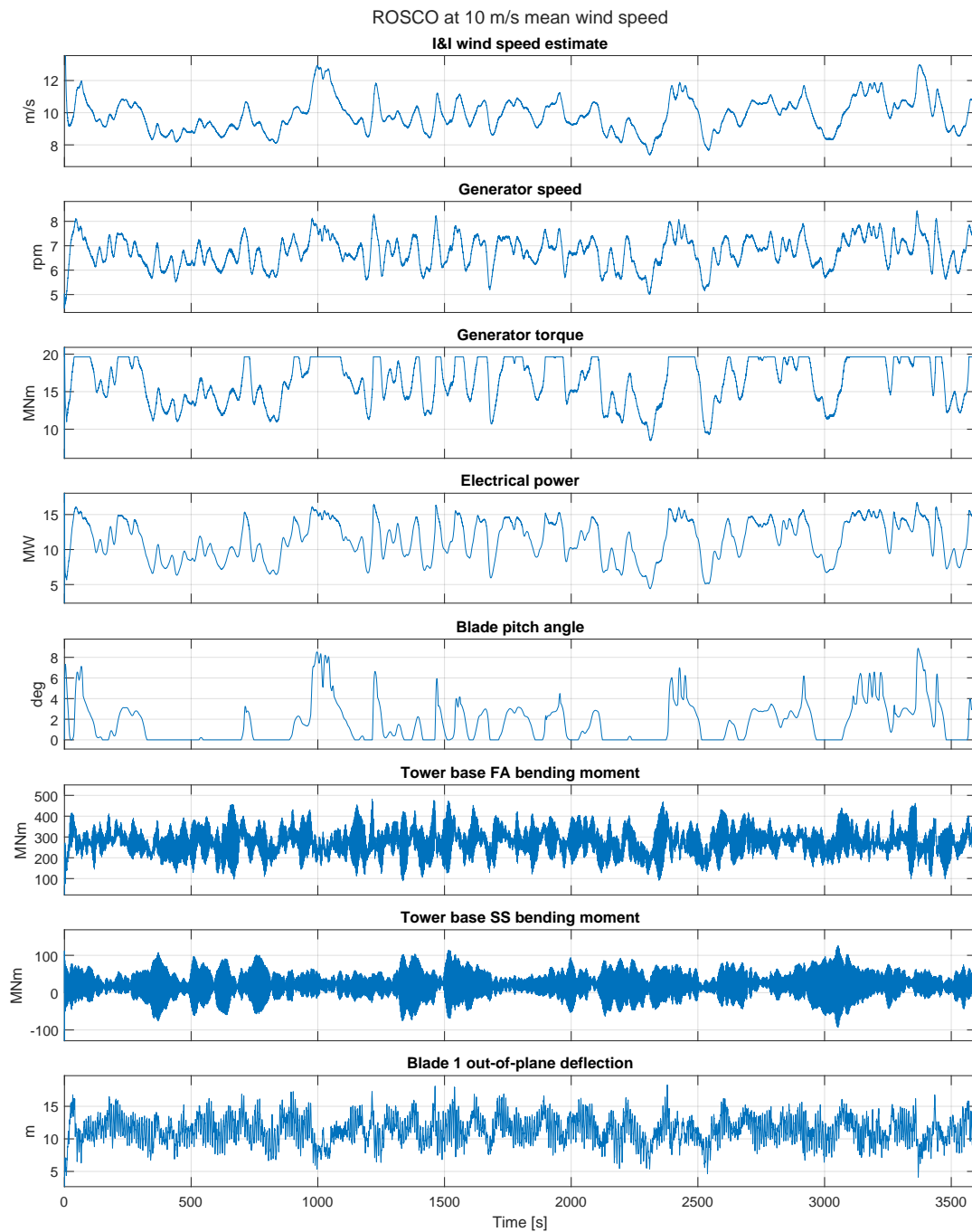
Figure 13. (a) First hour of the simulation at $10\,\mathrm{m\,s^{-1}}$ mean wind speed, ROSCO.
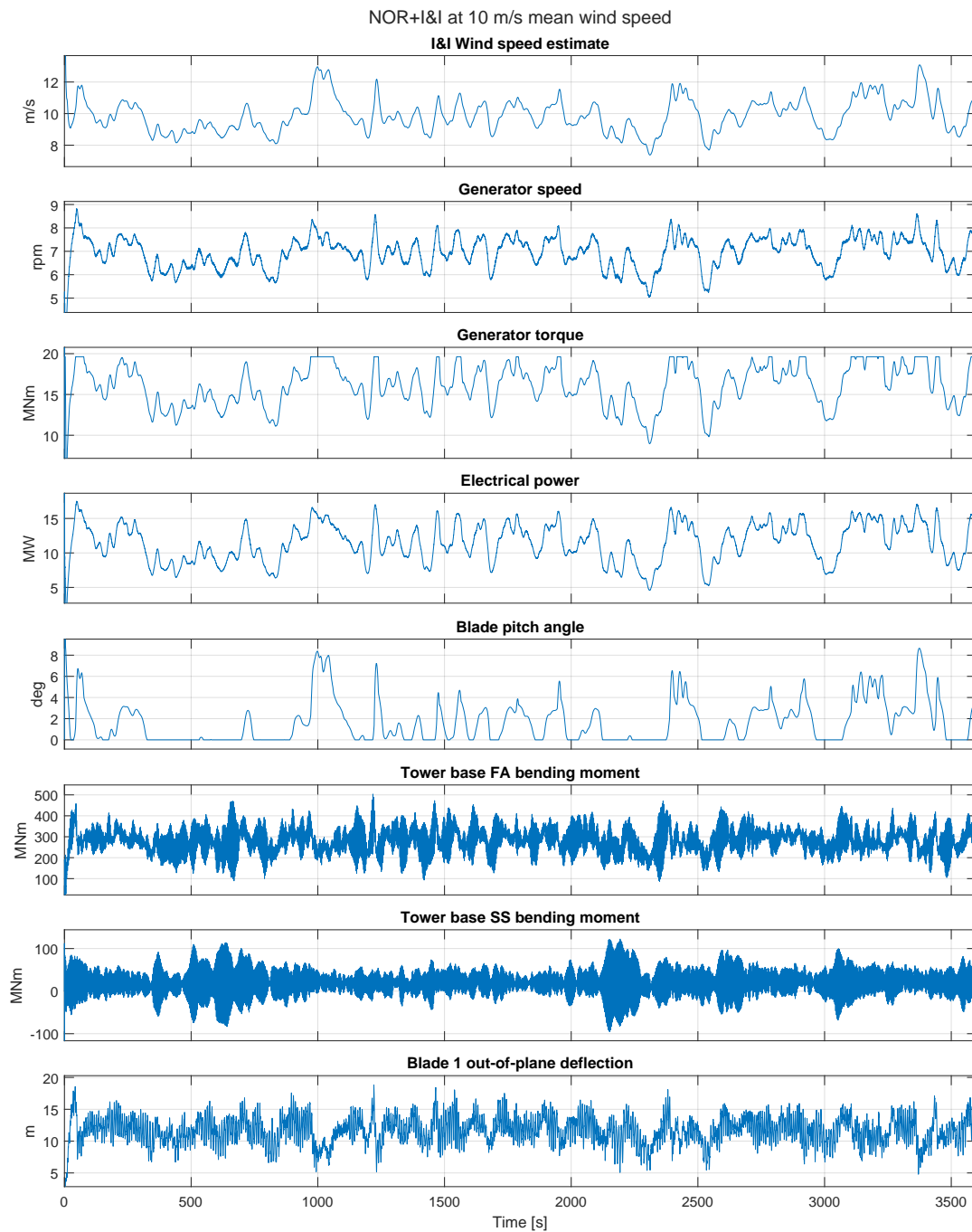
Figure 13. (b) First hour of the simulation at $10\,\mathrm{m\,s^{-1}}$ mean wind speed, NOR+I&I.
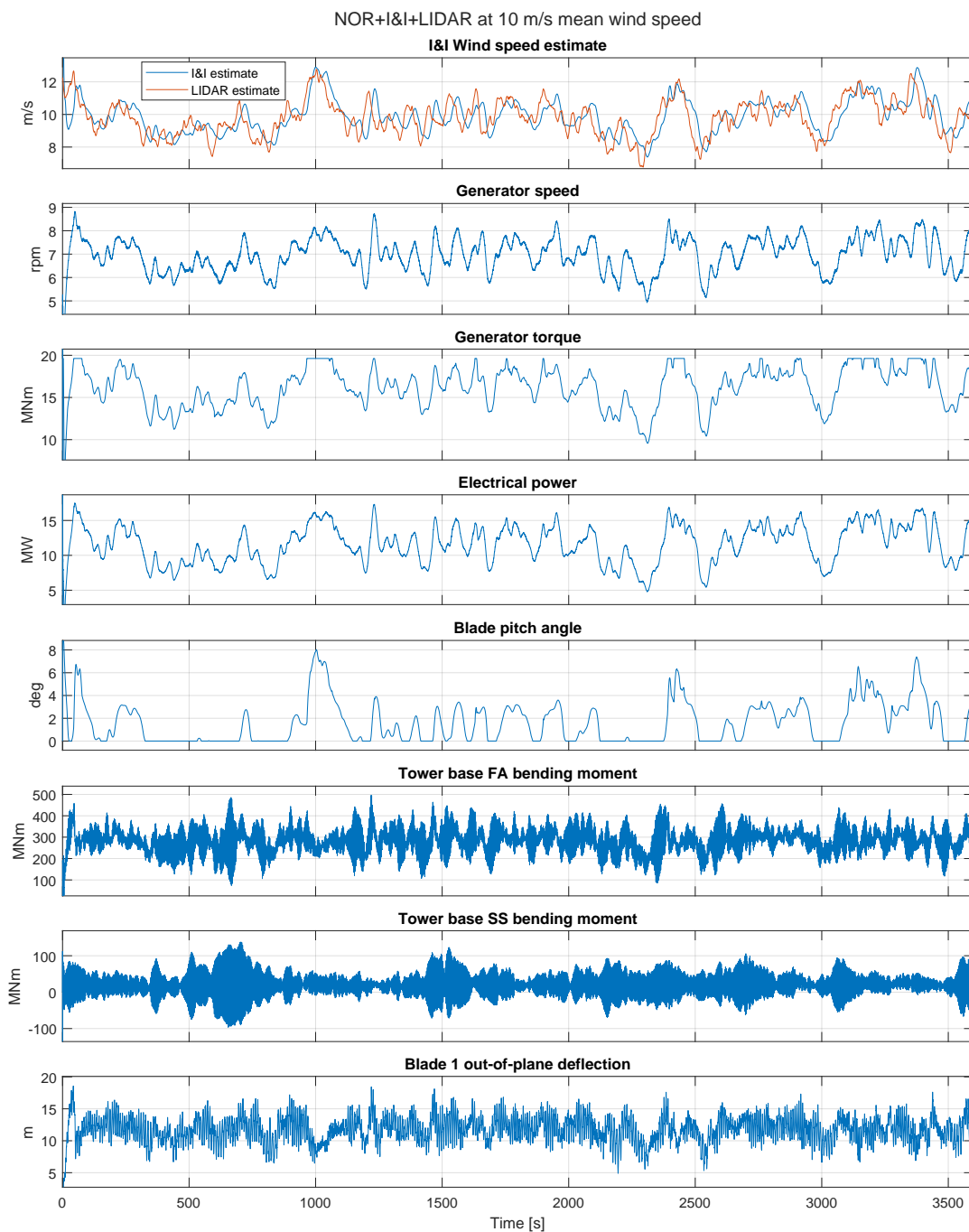
Figure 13. (c) First hour of the simulation at $10\,\mathrm{m\,s^{-1}}$ mean wind speed, NOR+I&I+LIDAR. The top diagram shows both the I&I and LIDAR estimates, the average of which is being used as wind speed estimate input to the NOR controller.

Appendix A: Robustness of NOR+I&I towards modelling errors

The combination of NOR and I&I is robust towards errors in the modelling of the aerodynamic torque, in the sense that there are no asymptotic tracking errors even if there is a model mismatch. The reasoning for this is presented in the following.

By substituting equation (30) or (32) into (25), it follows that

$$J\dot{\Omega} = M_a(\Omega, v_x, \theta) - M_a(\Omega, \hat{v}_x, \theta) + J\mu(\Omega_{\text{ref}} - \Omega). \tag{A1}$$

Generally, the NOR controller, because it relies on an aerodynamic torque model $M_a(\Omega, v_x, \theta)$, would be susceptible to discrepancies of that model from reality. However, the combination with the I&I estimator, which uses the same model for its wind speed estimate, compensates such errors. To see this, let $M_a(\Omega, v_x, \theta)$ be the real aerodynamic torque that the wind applies, and $\hat{M}_a(\Omega, v_x, \theta)$ be the (incorrect) model that NOR and I&I use. The dynamic equation for the I&I estimator is then

$$\dot{\hat{v}}_x = \frac{\kappa}{J}(M_a(\Omega, v_x, \theta) - \hat{M}_a(\Omega, \hat{v}_x, \theta)). \tag{A2}$$

Assume that the wind speed v_x is constant. Then $\hat{v}_x$ converges to some value $\hat{v}_x^\infty$, which is generally different from v_x. From (A2) it follows that

$$M_a(\Omega, v_x, \theta) = \hat{M}_a(\Omega, \hat{v}_x^\infty, \theta). \tag{A3}$$

Under the aerodynamic torque model $\hat{M}_a$ the closed loop becomes

$$J\dot{\Omega} = M_a(\Omega, v_x, \theta) - \hat{M}_a(\Omega, \hat{v}_x, \theta) + J\mu(\Omega_{\text{ref}} - \Omega). \tag{A4}$$

Using (A3) it follows that in the limit the closed loop has the dynamics

$$J\dot{\Omega} = J\mu(\Omega_{\text{ref}} - \Omega), \tag{A5}$$

which are stable and achieve perfect reference tracking despite the model discrepancy.

Intuitively, this robustness can be explained in the following way: If, for examples the power coefficients in $\hat{M}_a$ are higher than in reality, the I&I estimator underestimates the wind speed. The NOR controller computes the generator torque based on underestimated wind speed and overestimated power coefficient. These two effects compensate, and the correct aerodynamic torque is compensated.

Appendix B: Theoretical comparison between NOR and ROSCO

The combination of NOR controller and I&I estimator is a form of "pseudo-feedforward". This is because the I&I estimate is the output of the estimator dynamic system, which has the rotor speed as input. Thus a feedforward of the I&I estimate works similarly to a PI controller. This means that NOR+I&I is a essentially a feedback controller like ROSCO, formulated as feedforward.

In this appendix a connection between NOR+I&I and ROSCO is established, which allows for comparison and even conversion of the control architectures. With linearization, both lead to second order closed-loop dynamics, and the parameters of the controllers can be converted into one another. Then, NOR+I&I and ROSCO are fundamentally the same controller. However,
520   it will be seen that NOR+I&I has some advantages.

B1 Linearized NOR in either region

Consider an equilibrium $\Omega^*, v_x^*, \theta^*, M_g^*$ of (6). Denote the partial derivatives of the aerodynamic torque by

$$\alpha = \frac{\partial M_a(\Omega^*, v_x, \theta^*)}{\partial v_x}\bigg|_{v_x^*}, \tag{B1}$$

$$\beta = \frac{\partial M_a(\Omega^*, v_x^*, \theta)}{\partial \theta}\bigg|_{\theta^*}, \tag{B2}$$

525    $$\gamma = \frac{\partial M_a(\Omega, v_x^*, \theta^*)}{\partial \Omega}\bigg|_{\Omega^*}. \tag{B3}$$

The linearizations of the closed loop, the control law and the I&I estimator are

$$J\dot{\Omega} = \alpha\Delta v_x + \beta\Delta\theta + \gamma\Delta\Omega - \Delta M_g, \tag{B4}$$

$$\Delta M_g = \alpha\Delta\hat{v}_x + \beta\Delta\theta + \gamma\Delta\Omega + J\mu\Delta\Omega - J\mu\Delta\Omega_{\text{ref}}, \tag{B5}$$

$$\dot{\hat{v}}_x = \tilde{\kappa}(\Delta v_x - \Delta\hat{v}_x). \tag{B6}$$

530   Note that this is the case no matter if the controller is operating in Region 2 or 3. Substituting (B5) into (B4) leads to

$$J\dot{\Omega} = \alpha(\Delta v_x - \Delta\hat{v}_x) + J\mu(\Delta\Omega_{\text{ref}} - \Delta\Omega) \tag{B7}$$

$$= \alpha\tilde{\kappa}^{-1}\dot{\hat{v}}_x + J\mu(\Delta\Omega_{\text{ref}} - \Delta\Omega). \tag{B8}$$

Differentiating (B7) and using (B8) to replace $\dot{\hat{v}}_x$ yields

$$J\ddot{\Omega} = \alpha\dot{v}_x - \alpha\dot{\hat{v}}_x + J\mu(\dot{\Omega}_{\text{ref}} - \dot{\Omega}), \tag{B9}$$

535    $$J\ddot{\Omega} = \alpha\dot{v}_x - \tilde{\kappa}J\dot{\Omega} + J\mu(\Delta\Omega_{\text{ref}} - \Delta\Omega) + J\mu\tilde{\kappa}(\dot{\Omega}_{\text{ref}} - \dot{\Omega}). \tag{B10}$$

Rearranging and dividing by J gives the closed loop

$$\ddot{\Omega} + (\tilde{\kappa} + \mu)\dot{\Omega} + \tilde{\kappa}\mu\Delta\Omega = \alpha J^{-1}\dot{v}_x + \mu\dot{\Omega}_{\text{ref}} + \tilde{\kappa}\mu\Delta\Omega_{\text{ref}}. \tag{B11}$$

B2 Linearized ROSCO in Region 2

In Region 2 ROSCO uses a gain-scheduled PI controller of the form

540    $$\Delta M_g = K_P^g(\Omega_{\text{ref}} - \Omega) + K_I^g\int(\Omega_{\text{ref}} - \Omega)\mathrm{d}t. \tag{B12}$$

Inserting this into the linearized plant equation and differentiation lead to

$$J\ddot{\Omega} = \alpha\dot{v}_x + \gamma\dot{\Omega} + K_P^g(\dot{\Omega} - \dot{\Omega}_{\text{ref}}) + K_I^g(\Omega - \Omega_{\text{ref}}), \tag{B13}$$

and rearranged,

$$\ddot{\Omega} - \frac{K_P^g + \gamma}{J}\dot{\Omega} - \frac{K_I^g}{J}\Delta\Omega = \frac{\alpha}{J}\dot{v}_x - \frac{K_P^g}{J}\dot{\Omega}_{\text{ref}} - \frac{K_I^g}{J}\Omega_{\text{ref}}. \tag{B14}$$

545 **B3   Linearized ROSCO in Region 3**

Assume that the generator torque is set constantly to its rated value. The PI controller now takes the form

$$\Delta\beta = K_P^\theta(\Omega_{\text{ref}} - \Omega) + K_I^\theta \int (\Omega_{\text{ref}} - \Omega)\mathrm{d}t. \tag{B15}$$

Inserting this into (B4) and differentiation yield

$$J\ddot{\Omega} = \alpha\dot{v}_x + \gamma\dot{\Omega} + \beta K_P^\theta(\dot{\Omega}_{\text{ref}} - \dot{\Omega}) + \beta K_I^\theta(\Omega_{\text{ref}} - \Omega), \tag{B16}$$

550 and rearranged,

$$\ddot{\Omega} + \frac{\beta K_P^\theta - \gamma}{J}\dot{\Omega} + \frac{\beta K_I^\theta}{J}\Delta\Omega = \frac{\alpha}{J}\dot{v}_x + \frac{\beta K_P^\theta - \gamma}{J}\dot{\Omega}_{\text{ref}} + \frac{\beta K_I^\theta}{J}\Delta\Omega_{\text{ref}} \tag{B17}$$

B4   Parameter tuning for desired closed loop

We found that NOR+I&I and ROSCO lead to second order closed loop dynamics when linearized. This closed loop can be tuned using the controller and estimator gains. Let the closed-loop undamped natural frequency be ω_{des}, and the damping factor

555 be ζ_{des}. The desired left-hand side is then

$$\ddot{\Omega} + 2\zeta_{\text{des}}\omega_{\text{des}}\dot{\Omega} + \omega_{\text{des}}^2\Delta\Omega. \tag{B18}$$

The equations to tune the parameters of both controllers, obtained from equating this to the left-hand sides of (B11), (B14) and (B17), are then, for Region 2:

$$\begin{aligned}
2\zeta_{\text{des}}\omega_{\text{des}} &= \tilde{\kappa} + \mu = -\frac{K_P^g + \gamma}{J}, \\
\omega_{\text{des}}^2 &= \tilde{\kappa}\mu = -\frac{K_I^g}{J}.
\end{aligned} \tag{B19}$$

560 And for Region 3:

$$\begin{aligned}
2\zeta_{\text{des}}\omega_{\text{des}} &= \tilde{\kappa} + \mu = \frac{\beta K_P^\theta - \gamma}{J}, \\
\omega_{\text{des}}^2 &= \tilde{\kappa}\mu = \frac{\beta K_I^\theta}{J}.
\end{aligned} \tag{B20}$$

Note that the special case $\zeta_{\text{des}} = 1$ leads to $\tilde{\kappa} = \mu = \omega_{\text{des}}$.

With these equations, parametrizations of NOR+I&I and ROSCO can be converted into one another, such that the linearized closed loops are the same. The two controllers are then, if looked at in one Region in isolation, two sides of the same coin. While

565 ROSCO approaches the nonlinearity with gain-scheduling, where the gains are obtained from differentials of the aerodynamic torque, NOR+I&I directly works with the nonlinear aerodynamic torque model. By chain rule, the controllers result in the same closed loop.

Code and data availability. Code and data are available from http://doi.org/10.5281/zenodo.14523056

Author contributions. RM developed the NOR controller, the idea of averaging I&I and LIDAR estimates and the theoretical foundations
570 discussed in this article. He also contributed the majority of the code and conducted the simulations. RM was also the primary contributor
to the writing of the article. RS served in a supervisory role, proposed the research problem discussed in this article, and contributed to the
writing and revising of the article.

Competing interests. The authors declare that they do not have any competing interests.

Acknowledgements. The authors would like to thank Luke Woolcock for many fruitful discussions and guidance in developing the simulation
575 framework.

References

Abbas, N. J., Zalkind, D. S., Pao, L., and Wright, A.: A reference open-source controller for fixed and floating offshore wind turbines, Wind Energy Science, 7, 53–73, https://doi.org/10.5194/wes-7-53-2022, 2022.

Astolfi, A. and Ortega, R.: Immersion and invariance: a new tool for stabilization and adaptive control of nonlinear systems, IEEE Transactions on Automatic Control, 48, 590–606, https://doi.org/10.1109/TAC.2003.809820, 2003.

Astolfi, A., Karagiannis, D., and Ortega, R.: Nonlinear and Adaptive Control with Applications, 2008.

Balas, M., Lee, Y., and Kendall, L.: Disturbance tracking control theory with application to horizontal axis wind turbines, in: ASME Wind Energy Symposium, https://doi.org/10.2514/6.1998-32, 1998.

Bech, J. I., Hasager, C. B., and Bak, C.: Extending the life of wind turbine blade leading edges by reducing the tip speed during extreme precipitation events, Wind Energy Science, 3, 729–748, https://doi.org/10.5194/wes-3-729-2018, 2018.

Bianchi, F. D., Battista, H. D., and Mantz, R. J.: Wind Turbine Control Systems, Springer, 2007.

Bundesverband der Energie- und Wasserwirtschaft: Die Energieversorgung 2022 – aktualisierter Jahresbericht, Tech. rep., https://www.bdew.de/service/publikationen/jahresbericht-energieversorgung, 2023.

Fu, W., Guo, F., Schlipf, D., and Peña, A.: Feedforward pitch control for a 15 MW wind turbine using a spinner-mounted single-beam lidar, Wind Energy Science, 8, 1893–1907, https://doi.org/10.5194/wes-8-1893-2023, 2023.

Gaertner, E., Rinker, J., Sethuraman, L., Zahle, F., Anderson, B., Barter, G. E., Abbas, N. J., Meng, F., Bortolotti, P., Skrzypinski, W., et al.: IEA wind TCP task 37: Definition of the IEA 15-megawatt offshore reference wind turbine, Tech. rep., National Renewable Energy Lab.(NREL), Golden, CO (United States), 2020.

Gambier, A.: Control of Large Wind Energy Systems, Theory and Methods for the User, Springer, 2022.

Gao, S., Zhao, H., Gui, Y., Zhou, D., and Blaabjerg, F.: An Improved Direct Power Control for Doubly Fed Induction Generator, I E E E Transactions on Power Electronics, 36, 4672–4685, https://doi.org/10.1109/TPEL.2020.3024620, 2021.

IEC: Wind turbines-Part 1: Design requirements, IEC 61400-1, 3rd edition, Tech. rep., International Electrotechnical Commission, Geneva, Switzerland, 2005.

Jonkman, B. J.: TurbSim user's guide, Tech. rep., National Renewable Energy Lab. (NREL), Golden, CO (United States), https://www.nrel.gov/docs/fy06osti/39797.pdf, 2006.

Jonkman, J., Butterfield, S., Musial, W., and Scott, G.: Definition of a 5-MW reference wind turbine for offshore system development, Tech. rep., National Renewable Energy Lab. (NREL), Golden, CO (United States), https://www.nrel.gov/docs/fy09osti/38060.pdf, 2009.

Kipchirchir, E., Do, M. H., Njiri, J. G., and Söffker, D.: Prognostics-based adaptive control strategy for lifetime control of wind turbines, Wind Energy Science, 8, 575–588, https://doi.org/10.5194/wes-8-575-2023, 2023.

Kost, C., Shammugam, S., Fluri, V., Peper, D., Memar, A., and Schlegl, T.: Study: Levelized Cost of Electricity - Renewable Energy Technologies, https://www.ise.fraunhofer.de/en/publications/studies/cost-of-electricity.html, 2021.

Liu, X., Ortega, R., Su, H., and Chu, J.: Identification of nonlinearly parameterized nonlinear models: application to mass balance systems, in: Proceedings of the 48h IEEE Conference on Decision and Control (CDC) held jointly with 28th Chinese Control Conference, pp. 4682–4685, https://doi.org/10.1109/CDC.2009.5399817, 2009.

Luo, N., Vidal, Y., and Acho, L.: Wind Turbine Control and Monitoring, Springer, 2014.

Mahdizadeh, A., Schmid, R., and Oetomo, D.: LIDAR-Assisted Exact Output Regulation for Load Mitigation in Wind Turbines, IEEE Transactions on Control Systems Technology, 29, 1102–1116, https://doi.org/10.1109/TCST.2020.2991640, 2021.

Mordor Intelligence: China Wind Energy Market Size & Share Analysis - Growth Trends & Forecasts (2023 - 2028), https://www.mordorintelligence.com/industry-reports/china-wind-energy-market, (last access: 10 December 2024), 2024.

615 Munteanu, I., Bratcu, A., Cutululis, N., and Ceanga, E.: Optimal Control of Wind Energy Systems, Towards a Global Approach, Springer, 2008.

NREL: OpenFAST, Version 2.1.0, GitHub [code], https://github.com/openfast/openfast, (last access: 10 December 2024), 2019.

NREL: ROSCO Version 2.8.0, GitHub [code], https://github.com/NREL/ROSCO, (last access: 10 December 2024), 2021.

Ortega, R., Mancilla-David, F., and Jaramillo, F.: A globally convergent wind speed estimator for windmill systems, in: 50th IEEE Conference
620 on Decision and Control and European Control Conference, pp. 6079–6084, https://doi.org/10.1109/CDC.2011.6160544, 2011.

Ortega, R., Mancilla-David, F., and Jaramillo, F.: A globally convergent wind speed estimator for wind turbine systems, International Journal of Adaptive Control and Signal Processing, 27, 413–425, https://doi.org/10.1002/acs.2319, 2013.

Requate, N., Meyer, T., and Hofmann, R.: From wind conditions to operational strategy: optimal planning of wind turbine damage progression over its lifetime, Wind Energy Science, 8, 1727–1753, https://doi.org/10.5194/wes-8-1727-2023, 2023.

625 Saberi, A., Stoorvogel, A., and Sannuti, P.: Control of Linear Systems with Regulation and Input Constraints, Springer, https://doi.org/https://doi.org/10.1007/978-1-4471-0727-9, 2000.

Schlipf, D.: Lidar-assisted control concepts for wind turbines, Ph.D. thesis, Universität Stuttgart, 2016.

Schlipf, D., Schlipf, D. J., and Kühn, M.: Nonlinear model predictive control of wind turbines using LIDAR, Wind Energy, 16, 1107–1129, https://doi.org/https://doi.org/10.1002/we.1533, 2013.

630 Schlipf, D., Guo, F., Raach, S., and Lemmer, F.: A Tutorial on Lidar-Assisted Control for Floating Offshore Wind Turbines, in: 2023 American Control Conference (ACC), pp. 2536–2541, https://doi.org/10.23919/ACC55779.2023.10156419, 2023.

Soltani, M. N., Knudsen, T., Svenstrup, M., Wisniewski, R., Brath, P., Ortega, R., and Johnson, K.: Estimation of Rotor Effective Wind Speed: A Comparison, IEEE Transactions on Control Systems Technology, 21, 1155–1167, https://doi.org/10.1109/TCST.2013.2260751, 2013.

635 van Kuik, G. and Peinke, J.: Long-term Research Challenges in Wind Energy - A Research Agenda by the European Academy of Wind Energy, Springer, 2016.

Woolcock, L., Liu, V., Witherby, A., Schmid, R., and Mahdizadeh, A.: Comparison of REWS and LIDAR-based feedforward control for fatigue load mitigation in wind turbines, Control Engineering Practice, 138, 105 477, https://doi.org/https://doi.org/10.1016/j.conengprac.2023.105477, 2023.

640 Wright, A., Fingersh, L., and Balas, M.: Testing State-Space Controls for the Controls Advanced Research Turbine, in: 44th AIAA Aerospace Sciences Meeting and Exhibit, https://doi.org/10.2514/6.2006-604, 2006.

Wright, A. D.: Modern Control Design for Flexible Wind Turbines, Tech. Rep. NREL/TP-500-35816, National Renewable Energy Lab. (NREL), Golden, CO (United States), https://doi.org/10.2172/15011696, 2004.

Wright, A. D. and Fingersh, L. J.: Advanced Control Design for Wind Turbines; Part I: Control Design, Implementation,
645 and Initial Tests, Tech. Rep. NREL/TP–500–42437, National Renewable Energy Lab. (NREL), Golden, CO (United States), https://doi.org/10.2172/927269, 2008.

Yaakoubi, A. E., Bouzem, A., Alami, R. E., Chaibi, N., and Bendaou, O.: Wind turbines dynamics loads alleviation: Overview of the active controls and the corresponding strategies, Ocean Engineering, 278, 114 070, https://doi.org/https://doi.org/10.1016/j.oceaneng.2023.114070, 2023.

650   Yuan, Y. and Tang, J.: Adaptive pitch control of wind turbine for load mitigation under structural uncertainties, Renewable Energy, 105, 483–494, https://doi.org/https://doi.org/10.1016/j.renene.2016.12.068, 2017.